The Astrophysical Journal Supplement Series, 264:50 (24pp), 2023 February https://doi.org/10.3847/1538-4365/aca537

A Catalog of the Highest-energy Cosmic Rays Recorded during Phase I of Operation of the Pierre Auger Observatory

A. Abdul Halim[1], P. Abreu[2], M. Aglietta[3,4], I. Allekotte[5], P. Allison[6], K. Almeida Cheminant[7], A. Almela[8,9], J. Alvarez-Muñiz[10], J. Ammerman Yebra[10], G. A. Anastasi[3,4], L. Anchordoqui[11], B. Andrada[8], S. Andringa[2], C. Aramo[12], P. R. Araújo Ferreira[13], E. Arnone[3,14], J. C. Arteaga Velázquez[15], H. Asorey[8], P. Assis[2], M. Ave[16], G. Avila[17], E. Avocone[18,19], A. M. Badescu[20], A. Bakalova[21], A. Balaceanu[22], F. Barbato[18,23], J. Beatty[6], J. A. Bellido[1,24], C. Berat[25], M. E. Bertaina[3,14], X. Bertou[5], G. Bhatta[7], P. L. Biermann[26], P. Billoir[27], V. Binet[28], K. Bismark[8,29], T. Bister[13], J. Biteau[30], J. Blazek[21], C. Bleve[25], J. Blümer[31], M. Boháčová[21], D. Boncioli[18,19], C. Bonifazi[32,33], L. Bonneau Arbeletche[34], N. Borodai[7], J. Brack[35], T. Bretz[13], P. G. Brichetto Orchera[8], F. L. Briechle[13], P. Buchholz[36], A. Bueno[37], S. Buitink[38], M. Buscemi[39,40], M. Büsken[8,29], A. Bwembya[41,42], K. S. Caballero-Mora[43], L. Caccianiga[44,45], I. Caracas[46], R. Caruso[39,40], A. Castellina[3,4], F. Catalani[47], G. Cataldi[48], L. Cazon[10], M. Cerda[49], R. Cester[3,14], J. A. Chinellato[34], J. Chirinos[50], J. Chudoba[21], L. Chytka[51], R. W. Clay[1], A. C. Cobos Cerutti[8,52], R. Colalillo[12,53], A. Coleman[54], M. R. Coluccia[48], R. Conceição[2], A. Condorelli[23,18], G. Consolati[44,55], F. Contreras[17], F. Convenga[31], D. Correia dos Santos[56], C. E. Covault[57], M. Cristinziani[36], C. S. Cruz Sanchez[58], S. Dasso[59,60], K. Daumiller[31], B. R. Dawson[1], R. M. de Almeida[56], J. de Jesús[8,31], S. J. de Jong[41,42], J. R. T. de Mello Neto[33,61], I. De Mitri[18,23], J. de Oliveira[62], D. de Oliveira Franco[34], F. de Palma[48,63], V. de Souza[16], E. De Vito[48,63], A. Del Popolo[39,40], O. Deligny[64], L. Deval[8,31], A. di Matteo[3], M. Dobre[22], C. Dobrigkeit[34], J. C. D'Olivo[65], L. M. Domingues Mendes[2], A. Dorofeev[35], R. C. dos Anjos[66], J. Ebr[21], M. Eman[41,42], R. Engel[29,31], I. Epicoco[48,63], M. Erdmann[13], A. Etchegoyen[8,9], H. Falcke[41,42,67], J. Farmer[68], G. Farrar[69], A. C. Fauth[34], N. Fazzini[35], F. Feldbusch[70], F. Fenu[3,14], B. Fick[50], J. M. Figueira[8], A. Filipčič[71,72], T. Fitoussi[31], B. Flaggs[54], T. Fodran[41], T. Fujii[68,102], A. Fuster[8,9], C. Galea[41], C. Galelli[44,45], B. García[8,52], H. Gemmeke[70], F. Gesualdi[8,31], A. Gherghel-Lascu[22], P. L. Ghia[64], U. Giaccari[41], M. Giammarchi[44], J. Glombitza[13], F. Gobbi[49], F. Gollan[8], G. Golup[5], M. Gómez Berisso[5], P. F. Gómez Vitale[17], J. P. Gongora[17], J. M. González[5], N. González[73], I. Goos[5], D. Góra[7], A. Gorgi[3,4], M. Gottowik[10], T. D. Grubb[1], F. Guarino[12,53], G. P. Guedes[74], E. Guido[36], S. Hahn[8,31], P. Hamal[21], M. R. Hampel[8], P. Hansen[58], D. Harari[5], J. Harton[35], V. M. Harvey[1], A. Haungs[31], T. Hebbeker[13], D. Heck[31], C. Hojvat[75], J. R. Hörandel[41,42], P. Horvath[51], M. Hrabovský[51], T. Huege[31,38], A. Insolia[39,40], P. G. Isar[76], P. Janecek[21], J. A. Johnsen[77], J. Jurysek[21], A. Kääpä[46], K. H. Kampert[46], B. Keilhauer[31], A. Khakurdikar[41], V. V. Kizakke Covilakam[8,31], H. O. Klages[31], M. Kleifges[70], J. Kleinfeller[49], F. Knapp[29], J. Knapp[78,101], N. Kunka[70], C. Lachaud[79], B. L. Lago[80], N. Langner[13], M. A. Leigui de Oliveira[81], V. Lenok[29], A. Letessier-Selvon[27], I. Lhenry-Yvon[64], D. Lo Presti[39,40], L. Lopes[2], R. López[82], L. Lu[83], Q. Luce[29], J. P. Lundquist[71], A. Machado Payeras[34], D. Mandat[21], B. C. Manning[1], J. Manshanden[84], P. Mantsch[75], S. Marafico[64], F. M. Mariani[44,45], A. G. Mariazzi[58], I. C. Mariş[73], G. Marsella[39,85], D. Martello[48,63], S. Martinelli[8,31], O. Martínez Bravo[82], M. A. Martins[10], M. Mastrodicasa[18,19], H. J. Mathes[31], J. Matthews[86], G. Matthiae[87,88], E. Mayotte[46,77], S. Mayotte[77], P. O. Mazur[75], G. Medina-Tanco[65], J. Meinert[46], D. Melo[8], A. Menshikov[70], S. Michal[51], M. I. Micheletti[28], L. Miramonti[44,45], S. Mollerach[5], F. Montanet[25], L. Morejon[46], C. Morello[3,4], A. L. Müller[21], K. Mulrey[41,42], R. Mussa[3], M. Muzio[69], W. M. Namasaka[46], A. Nasr-Esfahani[46], L. Nellen[65], G. Nicora[89], M. Niculescu-Oglinzanu[22], M. Niechciol[36], D. Nitz[50], I. Norwood[50], D. Nosek[90], V. Novotny[90], L. Nožka[51], A Nucita[48,63], L. A. Núñez[91], C. Oliveira[16], M. Palatka[21], J. Pallotta[89], G. Parente[10], A. Parra[82], J. Pawlowsky[46], M. Pech[21], J. Pękala[7], R. Pelayo[92], E. E. Pereira Martins[8,29], J. Perez Armand[93], C. Pérez Bertolli[8,31], L. Perrone[48,63], S. Petrera[18,23], C. Petrucci[18,19], T. Pierog[31], M. Pimenta[2], M. Platino[8], B. Pont[41], M. Pothast[41,42], M. Pourmohammad Shavar[39,85], P. Privitera[68], M. Prouza[21], A. Puyleart[50], S. Querchfeld[46], J. Rautenberg[46], D. Ravignani[8], M. Reininghaus[29], J. Ridky[21], F. Riehn[2], M. Risse[36], V. Rizi[18,19], W. Rodrigues de Carvalho[41], J. Rodriguez Rojo[17], M. J. Roncoroni[8], S. Rossoni[84], M. Roth[31], E. Roulet[5], A. C. Rovero[60], P. Ruehl[36], A. Saftoiu[22], M. Saharan[41], F. Salamida[18,19], H. Salazar[82], G. Salina[87], J. D. Sanabria Gomez[91], F. Sánchez[8], E. M. Santos[93], E. Santos[21], F. Sarazin[77], R. Sarmento[2], R. Sato[17], P. Savina[83], C. M. Schäfer[31], V. Scherini[48,63], H. Schieler[31], M. Schimassek[31], M. Schimp[46], F. Schlüter[8,31], D. Schmidt[29], O. Scholten[38], H. Schoorlemmer[41,42], P. Schovánek[21], F. G. Schröder[31,54], J. Schulte[13], T. Schulz[31], S. J. Sciutto[58], M. Scornavacche[8,31], A. Segreto[39,94], S. Sehgal[46], S. U. Shivashankara[71], G. Sigl[84], G. Silli[8], O. Sima[22,100], R. Smau[22], R. Šmída[68], P. Sommers[95], J. F. Soriano[11], R. Squartini[49], M. Stadelmaier[21], D. Stanca[22], S. Stanič[71], J. Stasielak[7], P. Stassi[25], M. Straub[13], A. Streich[8,29], M. Suárez-Durán[73], T. Sudholz[1], T. Suomijärvi[30], A. D. Supanitsky[8], Z. Szadkowski[96], A. Tapia[97], C. Taricco[3,14], C. Timmermans[41,42], O. Tkachenko[31], P. Tobiska[21], C. J. Todero Peixoto[47], B. Tomé[2], Z. Torrès[25], A. Travaini[49], P. Travnicek[21], C. Trimarelli[18,19], M. Tueros[58], R. Ulrich[31], M. Unger[31], L. Vaclavek[51], M. Vacula[51], J. F. Valdés Galicia[65], L. Valore[12,53], E. Varela[82], A. Vásquez-Ramírez[91], D. Veberič[31], C. Ventura[61], I. D. Vergara Quispe[58], V. Verzi[87], J. Vicha[21], L. M. Villase nor Cendejas[82], J. Vink[98],

S. Vorobiov[71], C. Watanabe[33], A. A. Watson[78], A. Weindl[31], L. Wiencke[77], H. Wilczyński[7], D. Wittkowski[46], B. Wundheiler[8], P. Younk[99], A. Yushkov[21], O. Zapparrata[73], E. Zas[10], D. Zavrtanik[71,72], and M. Zavrtanik[71,72]
(The Pierre Auger Collaboration)

[1] University of Adelaide, Adelaide, SA, Australia
[2] Laboratório de Instrumentação e Física Experimental de Partículas (LIP) and Instituto Superior Técnico (IST), Universidade de Lisboa (UL), Lisboa, Portugal
[3] INFN, Sezione di Torino, Torino, Italy
[4] Osservatorio Astrofisico di Torino (INAF), Torino, Italy
[5] Centro Atómico Bariloche and Instituto Balseiro (CNEA-UNCuyo-CONICET), San Carlos de Bariloche, Argentina; spokespersons@auger.org
[6] Ohio State University, Columbus, OH, USA
[7] Institute of Nuclear Physics PAN, Krakow, Poland
[8] Instituto de Tecnologías en Detección y Astropartículas (CNEA, CONICET, UNSAM), Buenos Aires, Argentina
[9] Universidad Tecnológica Nacional—Facultad Regional Buenos Aires, Buenos Aires, Argentina
[10] Instituto Galego de Física de Altas Enerxías (IGFAE), Universidade de Santiago de Compostela, Santiago de Compostela, Spain
[11] Department of Physics and Astronomy, Lehman College, City University of New York, Bronx, NY, USA
[12] INFN, Sezione di Napoli, Napoli, Italy
[13] RWTH Aachen University, III. Physikalisches Institut A, Aachen, Germany
[14] Università Torino, Dipartimento di Fisica, Torino, Italy
[15] Universidad Michoacana de San Nicolás de Hidalgo, Morelia, Michoacán, Mexico
[16] Universidade de São Paulo, Instituto de Física de São Carlos, São Carlos, SP, Brazil
[17] Observatorio Pierre Auger and Comisión Nacional de Energía Atómica, Malargüe, Argentina
[18] INFN Laboratori Nazionali del Gran Sasso, Assergi (L'Aquila), Italy
[19] Università dell'Aquila, Dipartimento di Scienze Fisiche e Chimiche, L'Aquila, Italy
[20] University Politehnica of Bucharest, Bucharest, Romania
[21] Institute of Physics of the Czech Academy of Sciences, Prague, Czech Republic
[22] "Horia Hulubei" National Institute for Physics and Nuclear Engineering, Bucharest-Magurele, Romania
[23] Gran Sasso Science Institute, L'Aquila, Italy
[24] Universidad Nacional de San Agustin de Arequipa, Facultad de Ciencias Naturales y Formales, Arequipa, Peru
[25] Université Grenoble Alpes, CNRS, Grenoble Institute of Engineering, LPSC-IN2P3, F-38000 Grenoble, France
[26] Max-Planck-Institut für Radioastronomie, Bonn, Germany
[27] Laboratoire de Physique Nucléaire et de Hautes Energies (LPNHE), Sorbonne Université, Université de Paris, CNRS-IN2P3, Paris, France
[28] Instituto de Física de Rosario (IFIR)—CONICET/U.N.R. and Facultad de Ciencias Bioquímicas y Farmacéuticas U.N.R., Rosario, Argentina
[29] Karlsruhe Institute of Technology (KIT), Institute for Experimental Particle Physics, Karlsruhe, Germany
[30] Université Paris-Saclay, CNRS/IN2P3, IJCLab, Orsay, France
[31] Karlsruhe Institute of Technology (KIT), Institute for Astroparticle Physics, Karlsruhe, Germany
[32] International Center of Advanced Studies and Instituto de Ciencias Físicas, ECyT-UNSAM and CONICET, Campus Miguelete—San Martín, Buenos Aires, Argentina
[33] Universidade Federal do Rio de Janeiro, Instituto de Física, Rio de Janeiro, RJ, Brazil
[34] Universidade Estadual de Campinas, IFGW, Campinas, SP, Brazil
[35] Colorado State University, Fort Collins, CO, USA
[36] Universität Siegen, Department Physik—Experimentelle Teilchenphysik, Siegen, Germany
[37] Universidad de Granada and C.A.F.P.E., Granada, Spain
[38] Vrije Universiteit Brussels, Brussels, Belgium
[39] INFN, Sezione di Catania, Catania, Italy
[40] Università di Catania, Dipartimento di Fisica e Astronomia "Ettore Majorana", Catania, Italy
[41] IMAPP, Radboud University Nijmegen, Nijmegen, The Netherlands
[42] Nationaal Instituut voor Kernfysica en Hoge Energie Fysica (NIKHEF), Science Park, Amsterdam, The Netherlands
[43] Universidad Autónoma de Chiapas, Tuxtla Gutiérrez, Chiapas, Mexico
[44] INFN, Sezione di Milano, Milano, Italy
[45] Università di Milano, Dipartimento di Fisica, Milano, Italy
[46] Bergische Universität Wuppertal, Department of Physics, Wuppertal, Germany
[47] Universidade de São Paulo, Escola de Engenharia de Lorena, Lorena, SP, Brazil
[48] INFN, Sezione di Lecce, Lecce, Italy
[49] Observatorio Pierre Auger, Malargüe, Argentina
[50] Michigan Technological University, Houghton, MI, USA
[51] Palacky University, RCPTM, Olomouc, Czech Republic
[52] Universidad Tecnológica Nacional—Facultad Regional Mendoza (CONICET/CNEA), Mendoza, Argentina
[53] Università di Napoli "Federico II", Dipartimento di Fisica "Ettore Pancini", Napoli, Italy
[54] University of Delaware, Department of Physics and Astronomy, Bartol Research Institute, Newark, DE, USA
[55] Politecnico di Milano, Dipartimento di Scienze e Tecnologie Aerospaziali, Milano, Italy
[56] Universidade Federal Fluminense, EEIMVR, Volta Redonda, RJ, Brazil
[57] Case Western Reserve University, Cleveland, OH, USA
[58] IFLP, Universidad Nacional de La Plata and CONICET, La Plata, Argentina
[59] Departamento de Física and Departamento de Ciencias de la Atmósfera y los Océanos, FCEyN, Universidad de Buenos Aires and CONICET, Buenos Aires, Argentina
[60] Instituto de Astronomía y Física del Espacio (IAFE, CONICET-UBA), Buenos Aires, Argentina
[61] Universidade Federal do Rio de Janeiro (UFRJ), Observatório do Valongo, Rio de Janeiro, RJ, Brazil
[62] Instituto Federal de Educação, Ciência e Tecnologia do Rio de Janeiro (IFRJ), Brazil
[63] Università del Salento, Dipartimento di Matematica e Fisica "E. De Giorgi", Lecce, Italy
[64] CNRS/IN2P3, IJCLab, Université Paris-Saclay, Orsay, France
[65] Universidad Nacional Autónoma de México, México, D.F., Mexico
[66] Universidade Federal do Paraná, Setor Palotina, Palotina, Brazil
[67] Stichting Astronomisch Onderzoek in Nederland (ASTRON), Dwingeloo, The Netherlands
[68] University of Chicago, Enrico Fermi Institute, Chicago, IL, USA
[69] New York University, New York, NY, USA
[70] Karlsruhe Institute of Technology (KIT), Institut für Prozessdatenverarbeitung und Elektronik, Karlsruhe, Germany

[71] Center for Astrophysics and Cosmology (CAC), University of Nova Gorica, Nova Gorica, Slovenia
[72] Experimental Particle Physics Department, J. Stefan Institute, Ljubljana, Slovenia
[73] Université Libre de Bruxelles (ULB), Brussels, Belgium
[74] Universidade Estadual de Feira de Santana, Feira de Santana, Brazil
[75] Fermi National Accelerator Laboratory, Fermilab, Batavia, IL, USA
[76] Institute of Space Science, Bucharest-Magurele, Romania
[77] Colorado School of Mines, Golden, CO, USA
[78] School of Physics and Astronomy, University of Leeds, Leeds, UK
[79] Laboratoire AstroParticule et Cosmologie (APC), Université Paris 7, CNRS-IN2P3, Paris, France
[80] Centro Federal de Educação Tecnológica Celso Suckow da Fonseca, Nova Friburgo, Brazil
[81] Universidade Federal do ABC, Santo André, SP, Brazil
[82] Benemérita Universidad Autónoma de Puebla, Puebla, Mexico
[83] University of Wisconsin–Madison, Department of Physics and WIPAC, Madison, WI, USA
[84] Universität Hamburg, II. Institut für Theoretische Physik, Hamburg, Germany
[85] Università di Palermo, Dipartimento di Fisica e Chimica "E. Segrè", Palermo, Italy
[86] Louisiana State University, Baton Rouge, LA, USA
[87] INFN, Sezione di Roma "Tor Vergata", Roma, Italy
[88] Università di Roma "Tor Vergata", Dipartimento di Fisica, Roma, Italy
[89] Centro de Investigaciones en Láseres y Aplicaciones, CITEDEF and CONICET, Villa Martelli, Argentina
[90] Charles University, Faculty of Mathematics and Physics, Institute of Particle and Nuclear Physics, Prague, Czech Republic
[91] Universidad Industrial de Santander, Bucaramanga, Colombia
[92] Unidad Profesional Interdisciplinaria en Ingeniería y Tecnologías Avanzadas del Instituto Politécnico Nacional (UPIITA-IPN), México, D.F., Mexico
[93] Universidade de São Paulo, Instituto de Física, São Paulo, SP, Brazil
[94] Istituto di Astrofisica Spaziale e Fisica Cosmica di Palermo (INAF), Palermo, Italy
[95] Pennsylvania State University, University Park, PA, USA
[96] University of Łódź, Faculty of High-Energy Astrophysics, Łódź, Poland
[97] Universidad de Medellín, Medellín, Colombia
[98] Universiteit van Amsterdam, Faculty of Science, Amsterdam, The Netherlands
[99] Los Alamos National Laboratory, Los Alamos, NM, USA
Received 2022 October 11; revised 2022 November 21; accepted 2022 November 21; published 2023 February 7

Abstract

A catalog containing details of the highest-energy cosmic rays recorded through the detection of extensive air showers at the Pierre Auger Observatory is presented with the aim of opening the data to detailed examination. Descriptions of the 100 showers created by the highest-energy particles recorded between 2004 January 1 and 2020 December 31 are given for cosmic rays that have energies in the range 78–166 EeV. Details are also given on a further nine very energetic events that have been used in the calibration procedure adopted to determine the energy of each primary. A sky plot of the arrival directions of the most energetic particles is shown. No interpretations of the data are offered.

Unified Astronomy Thesaurus concepts: Ultra-high-energy cosmic radiation (1733); Cosmic ray showers (327); Experimental data (2371); Catalogs (205)

1. Introduction

The energy spectrum of cosmic rays extends to beyond 100 EeV. Where and how these particles, predominantly the nuclei of the common elements up to iron, are accelerated is one of the major puzzles of astroparticle physics. The flux above 50 EeV is about 0.5 particles per square kilometer per century, so that measuring their properties requires the detection of the cascades or *air showers* that the particles create in the atmosphere. In this paper, the methods used by the Pierre Auger Collaboration to obtain the arrival directions and energies of the 100 highest-energy particles in the range 78–166 EeV are outlined, and details of the main features of the air showers produced by the cosmic rays are presented. Phase I of operation of the observatory ended on 2020 December 31. It is thus timely to release a catalog to demonstrate the quality of the data that lie behind measurements of the energy spectrum, the distribution of arrival directions, and the mass of the highest-energy cosmic rays that have been reported elsewhere (Aab et al. 2014a, 2014b, 2017a, 2020a). The events discussed here are included in the data set recently used in a discussion of the arrival directions of events above 32 eV (Abreu et al. 2022).[103] No interpretations of the data are offered in this paper. Recent reviews, together with some interpretations, of data on high-energy cosmic rays can be found in Mollerach & Roulet (2018) and Alves Batista et al. (2019). A discussion of present data on the highest-energy cosmic rays is included in the US Community Study on the Future of Particle Physics 2021 (Coleman et al. 2023).

The structure of the paper is as follows. In Section 2, after a brief outline of the methods used to detect the highest-energy cosmic rays, the instrumentation of the Auger Observatory relevant to this paper is described. In Section 3, brief accounts of the techniques developed by the collaboration are given, including that used to assign the energy of the primary particle

[100] Also at University of Bucharest, Physics Department, Bucharest, Romania.
[101] Now at Deutsches Elektronen-Synchrotron DESY, Zeuthen, Germany.
[102] Now at Graduate School of Science, Osaka Metropolitan University, Osaka, Japan.

[103] Two events with energies close to 100 EeV, used in a recent study of mass composition (Yushkov 2019), are not included here, or in Abreu et al. (2022), as different selection criteria were adopted.

that initiates each air shower, or event. In Section 4, the catalog is described and some events within it are discussed in detail. These descriptions have been prepared to aid scrutiny of the complete sample publicly available at https://opendata.auger.org/catalog/. In Section 5, a sky map of the arrival directions of the events is shown.

2. The Detection of High-energy Cosmic Rays and the Pierre Auger Observatory

2.1. The Detection of High-energy Cosmic Rays

Above an energy of about 100 TeV, the flux of cosmic rays is so low that the size of detectors flown using balloons, or deployed in space, is insufficient for detecting useful numbers of primary particles directly. At higher energies, the particles create cascades, largely of electrons, positrons, photons, and muons, that propagate through the atmosphere as extensive air showers. Such showers can be detected through the charged particles and photons that reach ground level, and by observing light emitted from the atmosphere. Properties of the primary cosmic rays are inferred from studies of these showers.

If the incoming particle is a proton or an atomic nucleus, then, in the first interaction with a nucleus in the atmosphere (usually nitrogen or oxygen), hundreds of pions are created. The neutral pions decay rapidly into photons that initiate electromagnetic cascades through pair production, with the electrons and positrons subsequently producing bremsstrahlung radiation. The electromagnetic cascade grows until the rates of energy loss through these two processes are exceeded by the rate of energy loss by ionization. Charged pions interact with nuclei to produce additional pions that further enrich the cascade until their energy falls below ∼300 GeV when charged-pion decay becomes more probable than interaction with nuclei. The nucleons of the incoming primary lose, on average, about 50% of their energy in the first interaction, and in further similar interactions, thus enhancing the number of secondary particles in the shower. The charged particles and the accompanying photons spread out laterally because of scattering, and because of the transverse momentum of the particles produced in the collisions.

The shower of secondary particles can be detected in several ways. One method is to spread a number of detectors over the ground—currently scintillation counters or water Cherenkov detectors (WCDs) are the most widely adopted. At ∼1 PeV, the footprint of the shower is about 10^4 m^2, while, for the energies of interest here, the equivalent scale is many square kilometers. The number of detectors deployed in any shower array is, of necessity, a compromise dictated by cost.

The particles of the shower can be thought of as traveling at close to the speed of light in a slightly curved, disklike configuration similar to a giant dinner plate, with the density of particles falling off rapidly from the center of the disk. The falloff is described by a lateral distribution function (LDF), knowledge of which is important for the reconstruction of events. The zenith angle of a shower is determined with an accuracy of ∼1° from the times of arrival of the first particles in the shower disk at the detectors.

Other methods of shower detection make use of the fluorescence radiation that results from the excitation of molecules of atmospheric nitrogen by charged particles in the shower and of the Cherenkov light created as these particles cross the atmosphere. Fluorescence radiation is emitted isotropically and can be observed at large distances from the shower. Detection is technically demanding as only about 5.6 photons are emitted in the 300–400 nm band for each MeV of energy deposited (Ave et al. 2013). The challenge of detecting such light from a shower produced by a particle of ∼3 EeV at 15 km is akin to trying to observe a 5 W light bulb moving at the speed of light at this distance. By contrast, Cherenkov radiation is much brighter with around 30 photons emitted between 400 and 700 nm per meter of track (Galbraith 1958), with the light concentrated along the direction of travel of the shower and with a lateral spread dictated by that of the electrons. In the events described below, scattered Cherenkov light is a background that must be accounted for when reconstructing the properties of showers with fluorescence detectors (FDs).

Other aspects of shower detection specific to the Auger Observatory are discussed in Section 2.2.

2.2. The Pierre Auger Observatory

The Pierre Auger Observatory is the largest cosmic-ray detector ever constructed. It was designed to explore the properties of the highest-energy cosmic rays with unprecedented statistical precision and this objective has been achieved. The primary experimental targets were the determination of the energy spectrum, the distribution of arrival directions, and the mass composition of cosmic rays above ∼1 EeV. Studies of lower-energy cosmic rays, of particle physics, and of geophysical phenomena now form important additions to the scope of the project.

The observatory is located near the city of Malargüe, Mendoza Province, Argentina, between latitudes 35.0°S and 35.3°S and longitudes 69.0°W and 69.4°W. The mean altitude of the site is about 1400 m above sea level, corresponding to an atmospheric overburden of about 875 g cm^{-2}. The observatory comprises an installation of about 1600 WCDs, separated by 1500 m, laid out on a triangular grid over an area of 3000 km^2 (the surface detector, SD), and overlooked by an FD comprising four stations, each containing six telescopes, each with 440 photomultipliers and a 13 m^2 mirror. A map of the site showing the features relevant to this paper is presented in Figure 1. A detailed description of the instrumentation can be found in Aab et al. (2015a).

The WCDs (each 10 m^2 × 1.2 m) are used to measure the energy flow at the ground level carried by the flux of muons, electrons, positrons, and photons in the air showers generated by the primary particles. In near-vertical events, there are 10 times as many photons as electrons and positrons. There are, in turn, 10 times as many electrons as muons in these events. The average energy of the muons in a near-vertical shower is ∼1 GeV, while the mean energy of the entities of the electromagnetic component is ∼10 MeV. Thus, the electromagnetic radiation is largely absorbed in the 3.2 radiation lengths of the 1.2 m depth of the WCDs, whereas most of the muons pass straight through, losing energy only through ionization. The energy deposited in the water by the shower components is expressed in terms of the signal, measured using three 9 inch photomultipliers, from a muon traversing vertically and in terms of vertical-equivalent muons, or VEM, and corresponds to an energy deposit of ∼250 MeV. In a vertical shower produced by a particle of 10 EeV, the signal, $S(1000)$, at 1000 m from the densest region of the shower, called the *core*,

Figure 1. The layout of the Pierre Auger Observatory covering 3000 km^2. Each small dot corresponds to a WCD. FDs are located at Los Leones, Coihueco, Loma Amarilla, and Los Morados. The 30° azimuthal fields of view of the six telescopes at each site are shown by the radial lines emanating from them: the vertical reach of the telescopes extends to an elevation of 28°.6. Data are transmitted to the central laboratory, located at a campus in Malargüe, using a purpose-built communication network. The dashed lines show roads. Gaps in the layout of the array are due to difficulties with landowners. Steerable lasers (see text) are located at positions CLF and XLF.

is ∼40 VEM, and is roughly a 50/50 mixture of signals from muons and the electromagnetic component.

The times of arrival of particles at the WCDs are measured using GPS signals that are also exploited to locate the position of each detector to 20 and 50 cm in the horizontal and vertical directions, respectively. At the highest energies, the incoming direction can be determined to better than 0°.4 (Aab et al. 2020b).

The thickness of the shower disk (in nanoseconds) is defined as the time that it takes for the signal amplitude to grow from 10% to 50% (this time, $t_{1/2}$, is referred to as the risetime). In events that arrive nearly vertically, risetimes vary from a few nanoseconds close to the core to ∼300 ns at distances of ∼1 km, and decrease as the zenith angle increases.

The time profiles of the signals recorded with the WCDs have been used in several studies. It is possible to build observables that allow inferences to be made about the mass composition, and to probe hadronic interactions above the energies attained at the Large Hadron Collider, with a statistical sample of ∼81,000 events (Aab et al. 2017b). Additionally, searches for photons and neutrinos in the cosmic particle flux have been made (Aab et al. 2017c, 2019a). Above 60°, the risetimes of the signals are too fast to measure accurately with the electronics currently in use.

Measurements of the fluorescence light make possible a calorimetric estimate of the energy of the primary particle (Aab et al. 2020a) and provide a key tool used in the determination of the mass of the primary particles (Aab et al. 2014b). For such studies, it is essential to monitor the atmosphere and this is done using steerable lasers located at the positions marked CLF and XLF in Figure 1 (Abreu et al. 2012). These lasers are also used to make independent checks on the accuracy of the reconstruction of the arrival directions possible (Mostafá 2005).

Data taking began on 2004 January 1 with 154 WCDs and two fluorescence stations partly operational. Observations with the instrumentation of Figure 1 started in 2008 June and have been in progress ever since. The SD is operated almost continuously, while observations with the FD are restricted to clear dark nights. Phase I of the project was completed on 2020 December 31. Instrumentation used in other Phase I studies is described in Aab et al. (2015a). It is thus timely to release a catalog giving details of the extensive air showers produced by the highest-energy cosmic rays observed thus far. In addition to the detailed information on the 100 events of the highest energy recorded between 2004 January 1 and 2020 December 31, which are part of the set of events discussed by Abreu et al. (2022), nine events of slightly lower energy, used for energy calibration, have been included to increase the number of fluorescence events presented.

3. Reconstruction of Shower Parameters

The properties that can be determined most directly are the arrival direction and the energy of the primary particle that initiates each air shower. Estimating the mass of the incoming particle is more complex as it requires assumptions to be made about the hadronic physics associated with interactions of nucleons and pions and, at present, it is not possible to identify the mass of the primaries except on an average basis (e.g., Aab et al. 2014b). No discussion of measurements relating to mass determination is included in this paper. In the following sections, brief descriptions of the methods used to find the arrival directions and the energies are given.

3.1. Recording of the Data

Data from the SDs to be used in reconstruction are derived from a relatively complex triggering procedure described in Abraham et al. (2010a). Briefly, triggers from each station, tagged with the GPS time, are sent at a rate of ∼20 Hz to a computer located at the campus in Malargüe (Figure 1) via a purpose-built link for communications. The computer is used to search for spatial and temporal coincidences between triggers from the detectors. When a coincidence is found between at least three stations, the data from the triggered detectors are downloaded (Abraham et al. 2010a). In addition to the trigger time, the data include readouts from flash analog-to-digital converters (FADCs) associated with each of the three photomultipliers in the WCDs. The GPS time stamps have a precision of 12 ns, while the FADCs are 10 bit running at 40 MHz. From the FADC information, the amplitude and time structure of each signal are obtained.

Data from the FDs are recorded in a different manner (Abraham et al. 2010b). The telescopes at each of the four fluorescence stations are operated remotely from the Malargüe Campus or, since 2017, additionally from various locations around the world. The camera of each telescope contains 440 photomultipliers (pixels). The recording of signals and time stamps is completely independent of that used for the SDs. A very loose criterion of a localized pattern of four pulses in consecutive time order is adopted as the trigger at each fluorescence telescope. Those triggers where a shower track can be found are transmitted to the central computer, together with information on the geometry of the shower candidate.

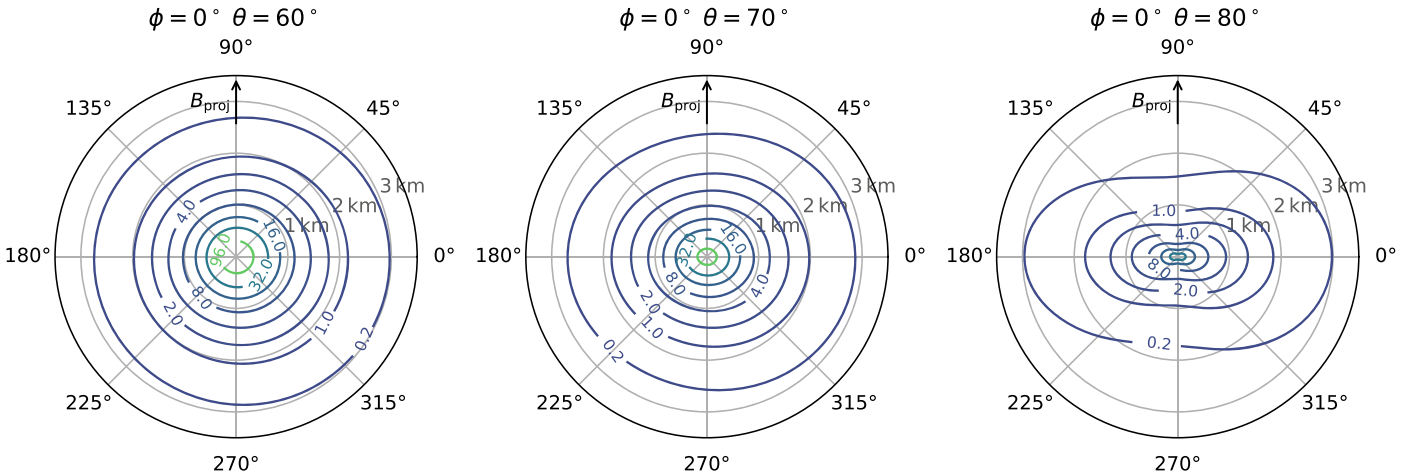

Figure 2. Parameterized densities of muons for a 10 EeV proton shower at zenith angles of 60°, 70°, and 80° arriving from an azimuth $\phi = 0°$. Radial units are in kilometers. The coordinate system is defined in the plane perpendicular to the shower direction with the y-axis parallel to the projection of the Earth's magnetic field, B_{proj}, on that plane. The magnitudes of the muon densities are indicated (32, 16, 8, ... per square meter).

From this information, the time of impact of the shower at a ground position in the region of the SDs is computed, so that all FADC traces in the region, arriving within 20 μs, are also centrally recorded. After each night of operation, data from the fluorescence triggers are then merged with those data collected with the SDs: these form the hybrid data set. For high-level analyses, several quality cuts are applied to the fluorescence events, including those relating to cloud cover and atmospheric aerosols. Further cuts are made to ensure that the selection of events is unbiased with respect to the primary particle mass (Aab et al. 2014a). The overall efficiency of these cuts is such that approximately 25% of SD events with energies above 10 EeV registered during FD operation have an accompanying good-quality and unbiased FD shower profile.

3.2. Reconstruction of the Arrival Direction and Energy of Showers

3.2.1. Introduction

While the reconstruction of the arrival direction of an air shower is relatively straightforward, as outlined in Section 3.2.2, the determination of the parameter of the shower to be adopted as a surrogate for the primary energy is more difficult. This is because, as the zenith angle increases, the shower loses the near-perfect circular symmetry found in an event generated by a cosmic ray entering the atmosphere at 0°. The loss of symmetry of the distribution of the signal size in the plane perpendicular to the arrival direction of a shower arises for several reasons: geometrical effects associated with the angles at which high-energy particles are emitted in early interactions, geometrical effects relating to the direction of travel of particles entering the detectors, attenuation—particularly of the electromagnetic component—as the shower crosses the array, and the effect of the geomagnetic field. The most direct experimental evidence of asymmetry is found in studies of the risetime of signals from the WCDs (Aab et al. 2016).

The consequences of asymmetries of the signal sizes have been studied in some detail using simulations. Luce et al. (2022) examined the impact on the electromagnetic component. At 1000 m from the shower axis, the amplitude of the asymmetry of the signal size is ∼50% in a shower produced by a primary of 10 EeV at a zenith angle of 45°. However, estimates of the parameter used to define the shower size (the signal size at 1000 m from the shower axis, $S(1000)$—see below) are changed by less than 10%. This is largely because the contribution of muons to the total signal in a detector rises with an increasing zenith angle.

At relatively small zenith angles, simulation studies have also been used to show that the effect of the geomagnetic field changes estimates of $S(1000)$ by only a few percent for angles around 45° (Abreu et al. 2011). However, as the zenith angle increases, the effect of this field becomes more evident because of the increasingly long path length of the muons as they cross the atmosphere. In Figure 2 the densities of muons reaching the ground, again estimated through simulation, are shown for three zenith angles.

It is evident that the asymmetry of the radial distribution of the muons in the shower increases with the zenith angle, becoming particularly apparent above 70°. At such angles, the electromagnetic part of the shower, arising predominantly from the decay of neutral pions, is largely absorbed as the atmospheric thickness exceeds 2440 g cm^{-2}. However, an electromagnetic component arising from muon bremsstrahlung, knock-on processes, and muon decay is present and is time-synchronous with the muons, so that the time spread of the signals is small, as will be seen in the events discussed in Section 4.

Novel methods have been developed to analyze events of large zenith angles (Ave et al. 2000; Aab et al. 2014c) as discussed in Section 3.2.3. There is, of course, no sharp transition between the zenith angle range in which atmospheric absorption dominates and that in which geomagnetic effects assume greater importance. Above ∼60° the accuracy of reconstruction of both the direction and energy is increasingly improved using the new techniques (Schmidt 2010), and accordingly different approaches are adopted above and below this zenith angle.

3.2.2. Reconstruction of Events with Zenith Angle <60°

The methods used to reconstruct events with zenith angles $\theta < 60°$ recorded by the WCDs are described in detail by Aab et al. (2020b). The zenith angle is measured from the zenith while the azimuth angle, ϕ, is measured counterclockwise from

east. For showers as large as those described here, all arrival directions are determined to better than 0.°4. Accordingly, as deflections by the Galactic magnetic field of protons exceed this number, even for the energies discussed here, no uncertainties are given. An uncertainty of 0.°4 in the zenith angle leads to an uncertainty in energy of <0.2%.

The positions of the detectors with respect to the core of the shower are found by fitting the observed signals to an LDF.[104] In general, because of the wide spacing of the detectors, it is not possible to determine this function for every event. Accordingly, an empirical description, based on the pioneering studies of Greisen (1956, 1960) and Kamata & Nishimura (1958), is adopted:

$$S_{\rm LDF}(r) = S(1000)\left[\left(\frac{r}{r_{\rm opt}}\right)\left(\frac{r + r_{\rm s}}{r_{\rm opt} + r_{\rm s}}\right)\right]^{\beta}$$

with $r_{\rm s}$ fixed at 700 m. The slope factor, β, is negative, changing from about −2.6 at $\theta = 0°$ to about −1.9 at 60°. The flattening of the LDF with an increasing angle is largely due to the increasing dominance of the muon component.

The quantity $r_{\rm opt}$ relates to the spacing of the detectors and is the distance at which uncertainties in the reconstructed signal size, arising from lack of knowledge of the LDF, are minimized (Hillas et al. 1971; Hillas 1977). For the detectors of the Auger Observatory, whose spacing is 1500 m, $r_{\rm opt}$ has been shown to be close to 1000 m (Newton et al. 2007). The signal size at this distance, $S(1000)$, is used to estimate the primary energy.

The average statistical uncertainty in the determination of $S(1000)$ at the highest energies is 8% (Aab et al. 2020b). The uncertainty on the impact point is ∼50 m. $S(1000)$ is influenced by changes in atmospheric conditions that affect the development of showers (Aab et al. 2017d), and by the geomagnetic field, which impacts the signal sizes in the shower (Abreu et al. 2011). Therefore, before the shower size estimator is used in the calibration procedure (Section 3.3), corrections of ∼2% and ∼1% are made for atmospheric and geomagnetic effects, respectively.

3.2.3. Reconstruction of Events with Zenith Angles >60°

The analysis of events with zenith angles >60° is important as extending measurements to these angles enhances the exposure of the observatory by 30%, and extends sky coverage to regions that would otherwise be inaccessible. However, as explained above, techniques different from those used to reconstruct showers arriving at smaller zenith angles must be adopted. Showers with zenith angles estimated to be as great as ∼90° have been recorded, but because the distance between detectors as seen by the shower is substantially shortened, the accuracy of reconstruction of the direction is badly degraded, and we restrict selection to those with $\theta < 80°$, where the directional uncertainties are <1°. The procedures developed to analyze these events are discussed in detail in Aab et al. (2014c).

Above 70° most of the particles at the detector level are energetic muons accompanied by an electromagnetic component in equilibrium with the muons arising from bremsstrahlung, knock-on electrons, and muon decay processes, which makes up 25% of the signal beyond ∼1 km from the core and around 30% within 1 km. Except at extreme distances, approximately 80% of the signal arrives within about 200 ns (see Figures 9 and 15 in Section 4 below). The muons travel tens to hundreds of kilometers before detection and are deflected significantly by the geomagnetic field. Thus, at ground level, the near-cylindrical symmetry associated with near-vertical events is lost, as shown in Figure 2.

For showers with an inclination between 60° and 70°, and in particular at distances closer than 1 km to the shower core, there is still a significant contribution from the electromagnetic component, 67% at 60° and 100 m, and accordingly this is included in the reconstruction (Valiño et al. 2010).

The number of stations satisfying the trigger conditions above 60° increases with $\sec\theta$ so that at 30 EeV the average number is ∼25 at 60°, while at 80° it is ∼45. The method used for reconstruction is based on fitting the signal pattern recorded to what is predicted from modeling the shower development. The muon signal scales with energy as $\rho_\mu(r) \propto E^\alpha$ with α in the range 0.90–0.95. The expected density of muons at the ground is given by $\rho_\mu(r) = N_{19}\rho_{\mu,19}(r, \theta, \phi)$, where N_{19}, chosen by convention, is a measure of shower size using a reference shower model and comparing the signals to those expected from simulated showers of 10 EeV with the same arrival direction. Simulations have shown that $\rho_{\mu,19}(r, \theta, \phi)$, at fixed zenith and azimuth angles, varies by only about 5% for changes in the energy and mass of the primary particle (Dembinski et al. 2010).

The absolute value of N_{19} depends on the choice of mass composition and hadronic model used in the simulation for the reference model, but the dependence is constant with energy and between the primaries (Aab et al. 2015b). This uncertainty does not impact the estimate of the primary energy because the constant shift is absorbed by the method used to determine the energy scale, as outlined in Section 3.3.

3.2.4. Reconstruction of Events Recorded with the FDs

The FDs provide calibration information from which the energies of the more abundant events obtained with the WCDs alone can be derived. Measurements of the fluorescence emission also give details on the longitudinal development of air showers in the atmosphere, including the determination of the depth at which the deposition of energy is greatest, that is, the shower maximum. This is a key measurement for mass estimation. Details of the reconstruction methods are discussed in Abraham et al. (2010b) and Aab et al. (2014a) with only a brief description given here.

The 440 pixels in each camera, illuminated by light from the air shower, are used to reconstruct a plane that includes the axis of the shower and the location of the telescope. Within this plane, a 3D reconstruction of the arrival direction is obtained by determining the geometry from the arrival times of the shower light at each pixel, and from the time of arrival of the shower particles at the WCD closest to the core

[104] When the core of a shower falls close to a detector, the signal can be so large that the electronic recording channels may saturate. This usually occurs for detectors within about 500 m of the core, where the signal is greater than 1000 VEM. An algorithm is used to estimate the true magnitude of the signal from the amplitude of the undershoot, which is introduced capacitatively. Moreover, for signals larger than 2000 VEM, the photomultiplier tube (PMT) response is highly nonlinear so that only timing information is used and the signal is treated in the LDF fit only as a lower limit to the actual size of the signal. Note that the estimated true signal value is used in the LDF fit for saturated signals smaller than 2000 VEM. For 50% of the events contained in the full data set, the signal in one station is saturated; three of the events discussed below have two saturated stations. Examples of saturated signals can be found in Section 4, and in the larger database.

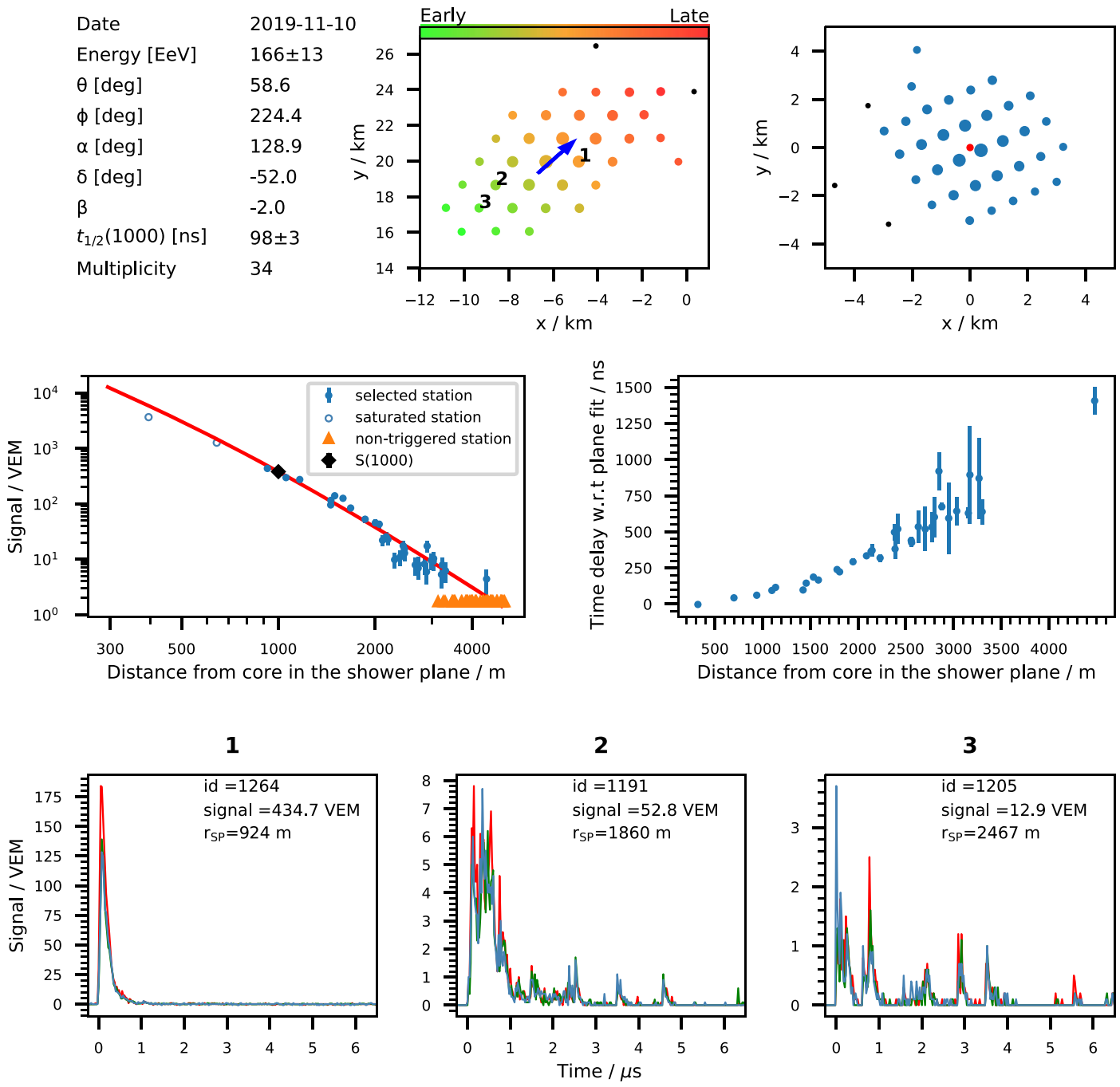

Figure 3. Features of the most energetic event (PAO191110, #1) recorded with the SD of the Pierre Auger Observatory. See text for details.

of the shower. This hybrid technique, implemented for the first time at the Auger Observatory, enhances the precision with which the shower geometry is determined: the direction is known to $\sim 0.^{\circ}6$ (Bonifazi 2009). The signal from each pixel is recorded in 100 ns intervals and the time and amplitude data are used to delineate the profile of the shower development using the techniques described by Unger et al. (2008). This method allows differentiation between the various sources of detected light, namely the fluorescence light, direct Cherenkov light, and light scattered from the Cherenkov beam into the fluorescence telescope from air molecules and aerosols.

For each 100 ns interval, the energy deposited in the slant depth interval corresponding to the measured light flux is estimated. These individual estimates are fitted using the universal shower profile function described in Andringa et al. (2011),

$$f(X) = \left(\frac{dE}{dX}\right)_{\max} \left(1 + \frac{R}{L}(X - X_{\max})\right)^{1/R^2} \exp\left(-\frac{X - X_{\max}}{RL}\right),$$

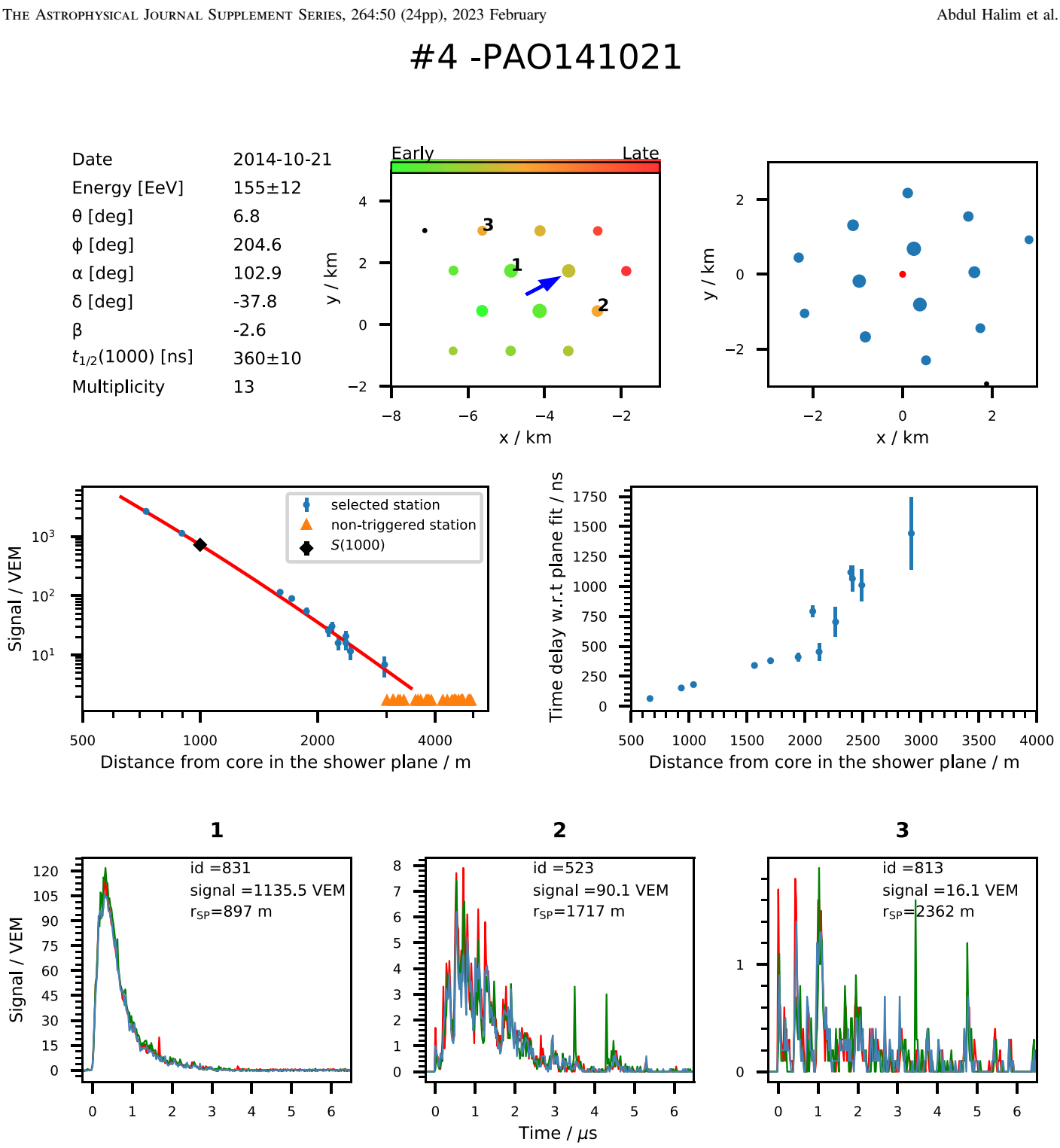

Figure 4. Features of a vertical event with a reconstructed energy of 155 EeV (PAO141021, #4). See text for details.

where $f(X)$ is the energy deposit in the slant depth X and $(dE/dX)_{\max}$ is the energy deposit at shower maximum. $X_{\max}$ is the slant depth of the maximum of the energy deposit, while R and L are the shape parameters loosely constrained in the fit to the average of the measured values (Dawson 2020). The universal shower profile function is a recasting of the Gaisser–Hillas functional form (Gaisser & Hillas 1977): its adoption diminishes correlations between shape parameters.

The energy of each event ($E_{\rm FD}$) is determined by integration under the area defined by the longitudinal profile, $f(X)$, that defines the rise and fall of the deposition of energy by the shower in the atmosphere, with the addition of 20% at 0.1 EeV and 12% at 100 EeV, respectively. This augmentation accounts for energy that is not deposited in the atmosphere but is carried into the ground largely by muons and neutrinos. The model-independent methods of determining this factor are discussed in Aab et al. (2019b). Above 10 EeV, the energy is determined

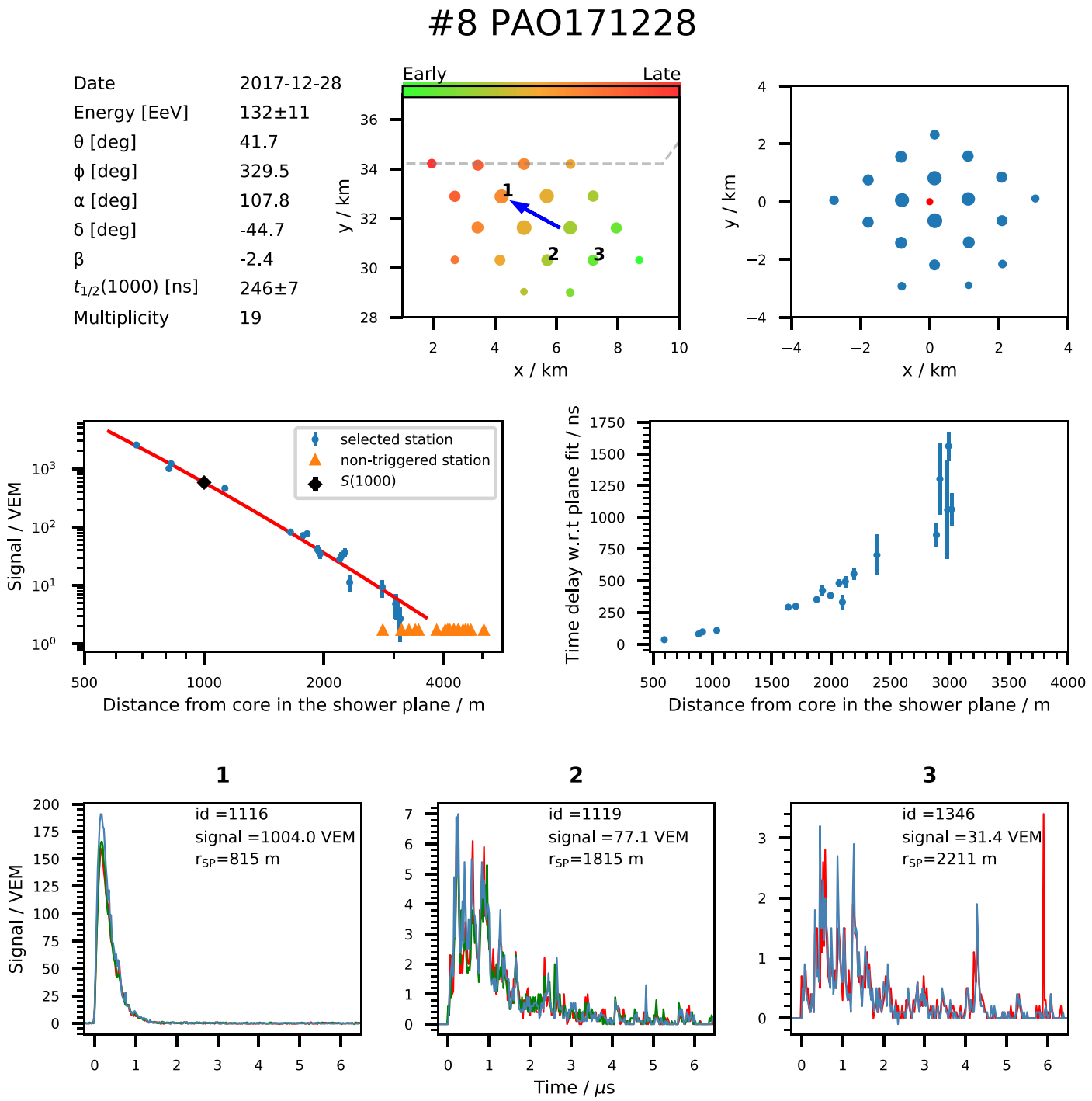

Figure 5. Features of an event (PAO171228, #8) recorded with WCDs located at one of the boundaries of the SD. See text for details. Note that in detector #1346 only two of the three photomultipliers were operational. Reality dictates that it is impossible to keep all three photomultipliers operational 100% of the time. Failures of two, or even all three, photomultipliers inevitably occur. Typically 98% of all stations are active at any time, sending triggers at 20 Hz to the central station (Section 3.1).

with a statistical precision of 8% and with a systematic uncertainty of ∼14% (Dawson 2020).

3.3. Determination of the Energy of the Primary Particles

The methods by which data from the SDs are calibrated to obtain the energies of the primaries are detailed in Aab et al. (2020a). Use is made of hybrid events, both for showers with $\theta < 60^\circ$ (referred to as "vertical events") and for events of larger zenith angles ("inclined events").

For vertical events, the measure of $S(1000)$ is first adjusted to the value that a shower would have if it arrived at 38° from the vertical, S_{38}, as this is the median zenith angle for the vertical sample. Using the 3338 hybrid events that are available, the calibration relationship is $E_{FD} = A\, S_{38}^{B}$, with $A = (0.186 \pm 0.003)$ EeV and $B = 1.031 \pm 0.004$. The calibration constants A and B are then used to estimate the energy for all SD events, E_{SD}. The statistical uncertainty of E_{SD}, obtained by propagating the errors on A and B, is 1% at the energies considered in this

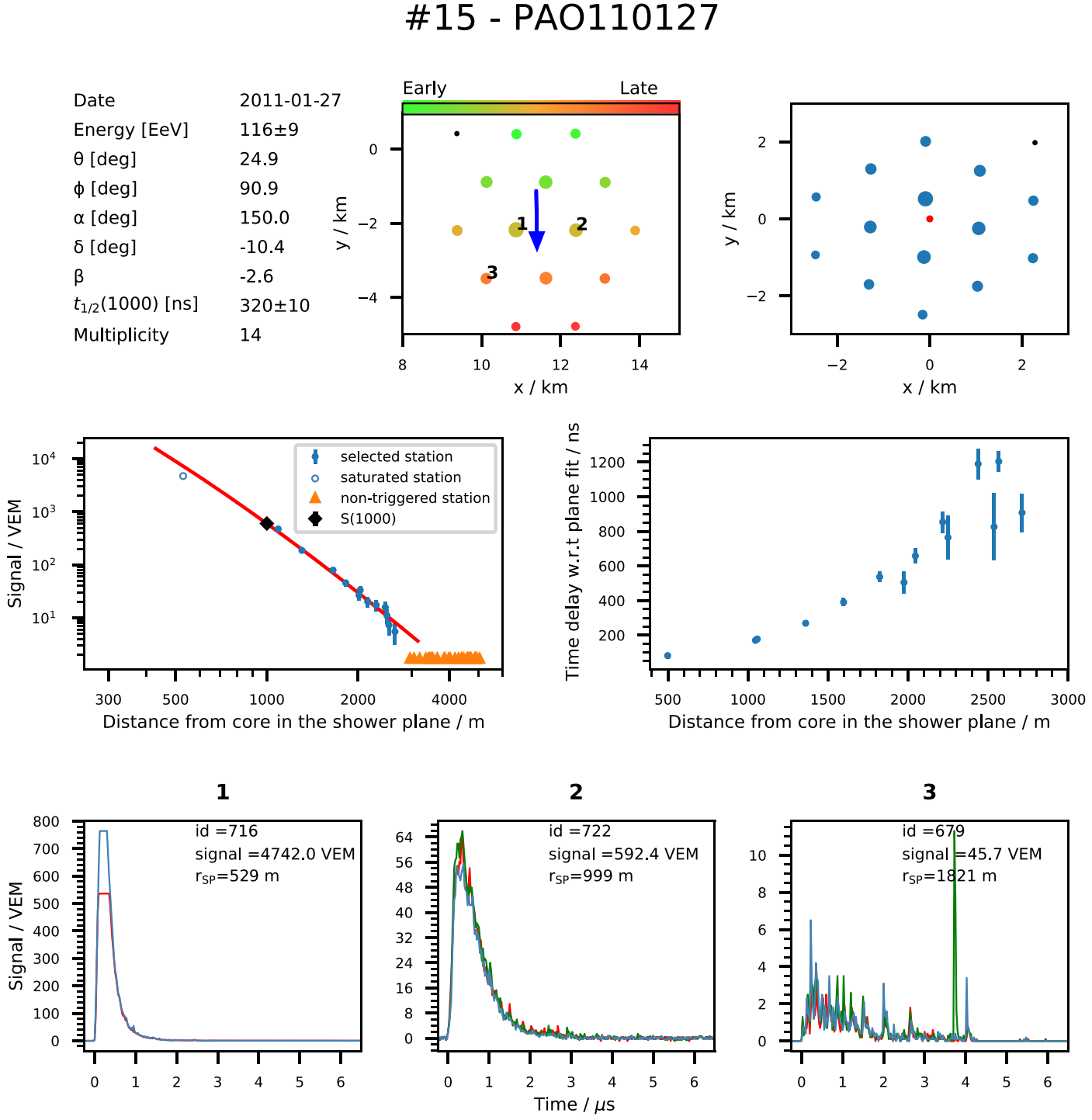

Figure 6. Features of an event (PAO110127, #15) in which one of the WCDs is saturated. See text for details.

paper. The energy resolution, obtained from the spread of E_{SD} values at a given E_{FD} in the calibration events, is ∼8% at the highest energies (Aab et al. 2020a).

A similar calibration procedure is adopted for events with $\theta > 60°$. Here the calibration is made using N_{19} as a surrogate for the shower size. The value of N_{19} is then adjusted to the value ($N_{19,68}$) for a shower arriving with 68°, the median zenith angle of the sample. The calibration is made with 389 events and the values of A and B are $A = (5.32 \pm 0.07)$ EeV and $B = 1.05 \pm 0.02$, where N_{19} replaces S_{38}. The smaller number of events available for evaluation of the energy of the more inclined events arises from the higher energy threshold required (4 EeV against 3 EeV), and from a requirement that the shower maximum be in the field of view of the FD telescopes. For inclined events the maximum is very distant from the impact point, effectively placing an upper limit on the zenith angle of ∼73° for both to be observable. For these events, the energy resolution is estimated to be 12%, at the highest energies, from a comparison of N_{19} with E_{FD} (Pierre Auger Collaboration, in preparation).

For hybrid events, two estimates of the energy are available, namely that from the one or more fluorescence measurements,

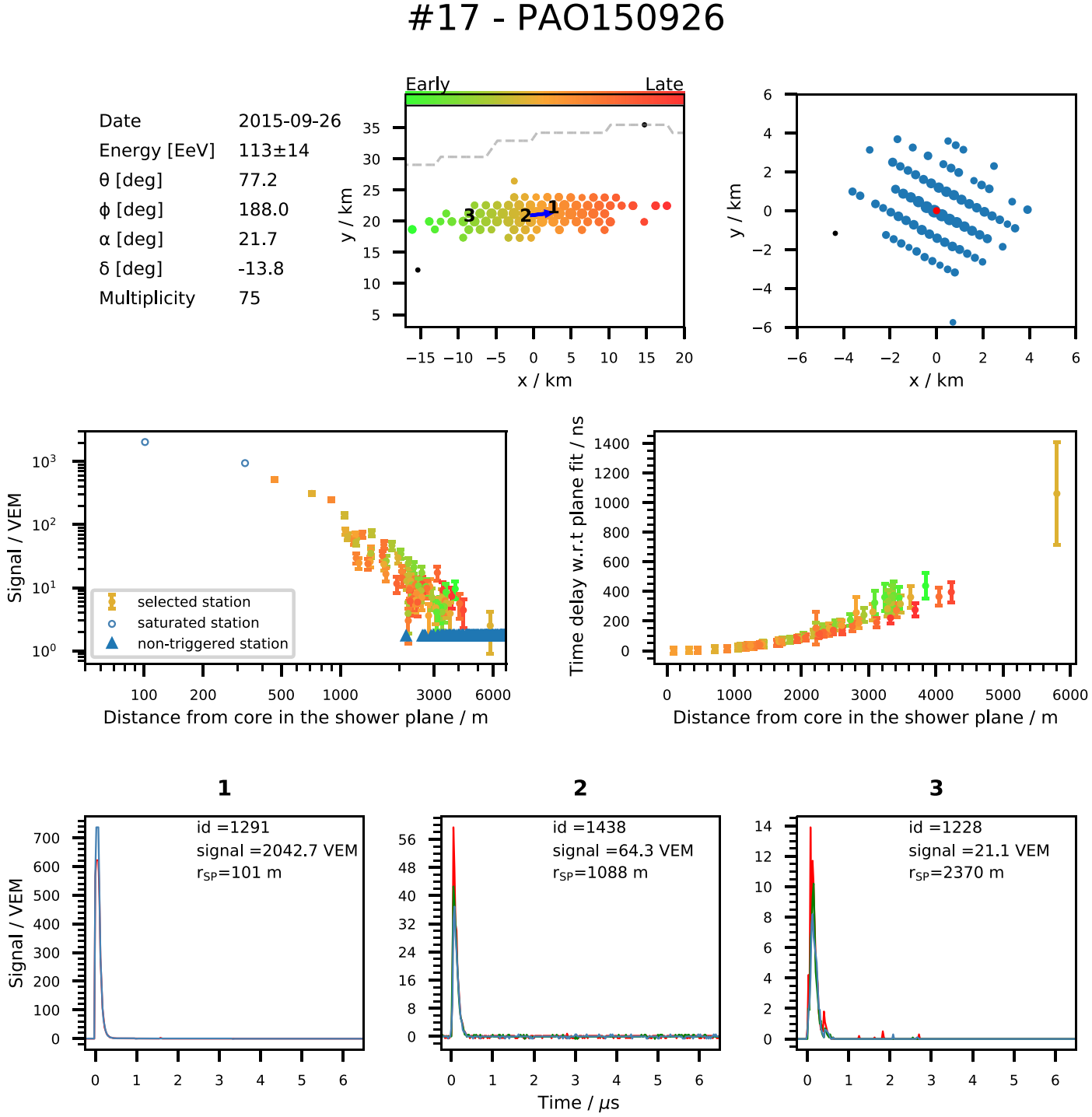

Figure 7. Features of the most energetic event (PAO150926, #17) belonging to the set of inclined showers ($\theta > 60°$). See text for details.

and that from the determination of $S(1000)$ and the use of the calibration data. For consistency, the latter value is quoted in all cases as it is available for all events. Average uncertainties in energy of 8% for vertical events and 12% for inclined events are given. The systematic uncertainty in the energy estimates coming from $S(1000)$ depends on the distance spread of the signals in an event and on the presence, or otherwise, of saturated stations. The dominant systematic uncertainty in the energy estimates of 14% comes from the FD measurements.

4. The Events of the Catalog

The catalog presented in this paper contains details of the 100 highest-energy events recorded using the array of WCDs of the Pierre Auger Observatory, together with similar data for a further nine events used in the energy calibration procedures outlined in Section 3.3. Full details of all 109 events are available at https://opendata.auger.org/catalog/. A list summarizing the events is also included there. In this section, features of eight exemplary events are discussed in some detail

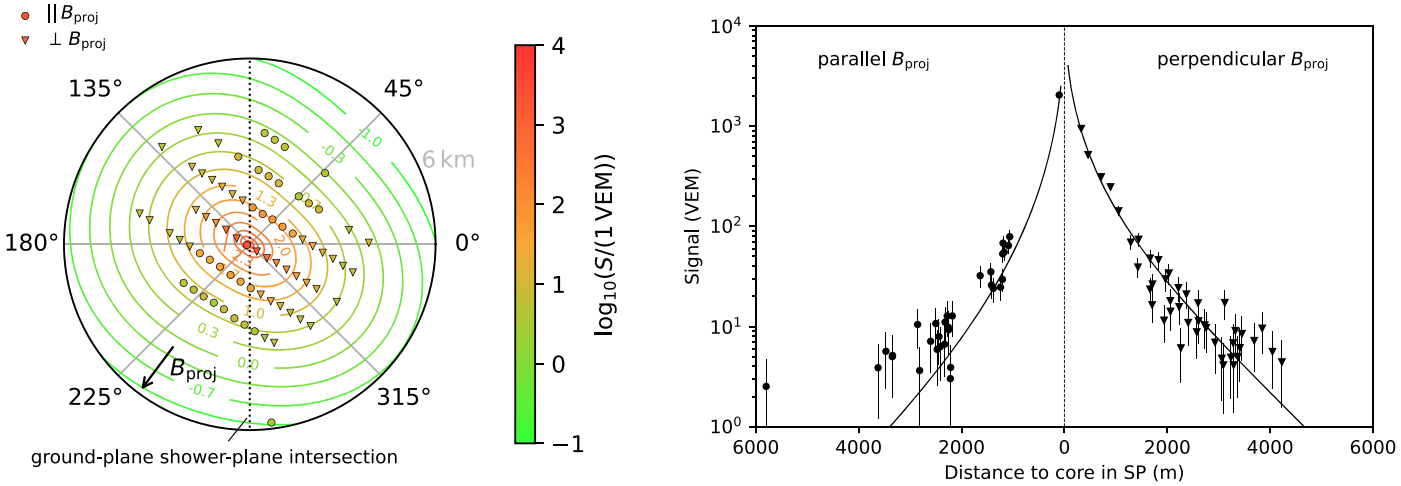

Figure 8. Left: 2D distribution of measured and expected signals in the shower plane. Station markers are colored according to the signal. The direction of the magnetic field in the shower plane (B_{proj}) is indicated by the black arrow. Triangular markers are stations that, as seen from the position of the core, lie within ±45° of the direction perpendicular to B_{proj}. That is, these stations are in the direction of the deflection that charged particles experience in the magnetic field. More particles therefore reach those stations (enhancing the signal) compared to those in stations that are at the same distance to the core but lie along the direction of the magnetic field (circular markers). The intersection of the shower plane with the ground plane is shown by the dashed line. Right: Projection of the signal distributions as a function of the distance from the shower core. The markers show the signal measured at the stations, while the curves show the expected signal. Stations in the direction parallel to the magnetic field are shown on the left, with stations in the direction perpendicular to the magnetic field shown on the right.

to facilitate appreciation of features in the full set of data. One of the two hybrid events discussed below has an energy lying just outside of the range of the top 100.

The events are identified with a catalog number (#N) that can be used to locate them in the depository, and by a name, PAOyymmdd, that indicates the year, month, and day of detection.

4.1. Description of Individual Events

4.1.1. Vertical Events

PAO191110 (#1). Some properties of the most energetic air shower registered with the SD are shown in Figure 3. The primary energy is (166 ± 13) EeV with the shower impacting the surface array at a zenith angle θ of 58.°6. It has an R.A. α of 128.°9 and a decl. δ of −52.°0. The top middle panel shows the event footprint on the ground, which spans an area of approximately (13 × 6) km^2, with 34 WCDs triggered. Black dots correspond to stations that are triggered randomly. The detectors struck are shown in a plane perpendicular to the direction of arrival in the top right-hand panel, where the red point corresponds to the position of the shower core. The color coding (and the blue arrow) shows the direction of propagation of the air shower, evolving from green for detectors that are triggered early to red for those that are triggered later. The radius of each circle is proportional to $\log S$, where S is the signal size measured in VEM.

In the left middle panel, the lateral distribution of the recorded signals, as a function of the distance to the shower core, is shown. The triggered (blue circles) and nontriggered stations (orange triangles) are indicated. The event has two saturated stations (blue open circles) close to the shower core. Events with two saturated detectors are rare occurrences: only three events in the full data sample have two detectors that are saturated simultaneously. The lateral spread of the signals is described by the modified Nishimura–Kamata–Greisen (NKG) LDF discussed in Section 3.2.1. The value of the exponent β in the LDF is given in the top left panel. In the right middle panel, the time delays with respect to a fit that assumes a plane shower front are shown for the triggered stations. The delays are measured in nanoseconds.

In the bottom three panels, the arrival time distributions of the signals recorded at three detectors (marked 1 to 3 on the signal map) are displayed. The different colors indicate the signals from the three photomultipliers in each detector. These traces exemplify how signal shapes vary with respect to the distance from the shower core. Here, and below, detectors are selected that lie close to the distance (1000 m) used to define the shower size (Section 3.2.2), and at other distances, selected according to the features being illustrated. It is known from direct measurements (Linsley & Scarsi 1962) that, except within a few meters of the shower axis, muons precede the electromagnetic component. The arrival times of the two components overlap to some extent, but the electromagnetic component lags behind the muon signals by an amount that increases with distance from the shower core. At 1000 m, the risetime, $t_{1/2}(1000)$, in this event is close to 100 ns (Section 3.2). The muons that are detected are typically minimum ionizing particles; as a result their signals show a fast risetime and a decay time that confines the signals over one to three 25 ns time bins. As the distance to the shower core increases, there is more dispersion of the shower particles, with smaller signals that are spread out in time.

PAO141021 (#4). An event of primary energy (155 ± 12) EeV arriving at the ground level at quasi-normal incidence (the measured zenith angle is 6.°8) is shown in Figure 4. The footprint of the event is more compact and less elongated than that of PAO191110 (#1). The top middle panel shows the footprint on the ground, which spans an area of approximately (6 × 3) km^2: 13 WCDs are triggered. The middle panels show the lateral distribution of the recorded signals as a function of the distance to the shower core on the left, and on the right, the time delays with respect to a plane shower front perpendicular to the incoming direction of the shower.

The signals and arrival times (bottom panels) of the particles recorded at the three selected detectors are markedly different from those selected for event PAO191110 (#1). The station with the largest signal (at 897 m from the core) has above 1000

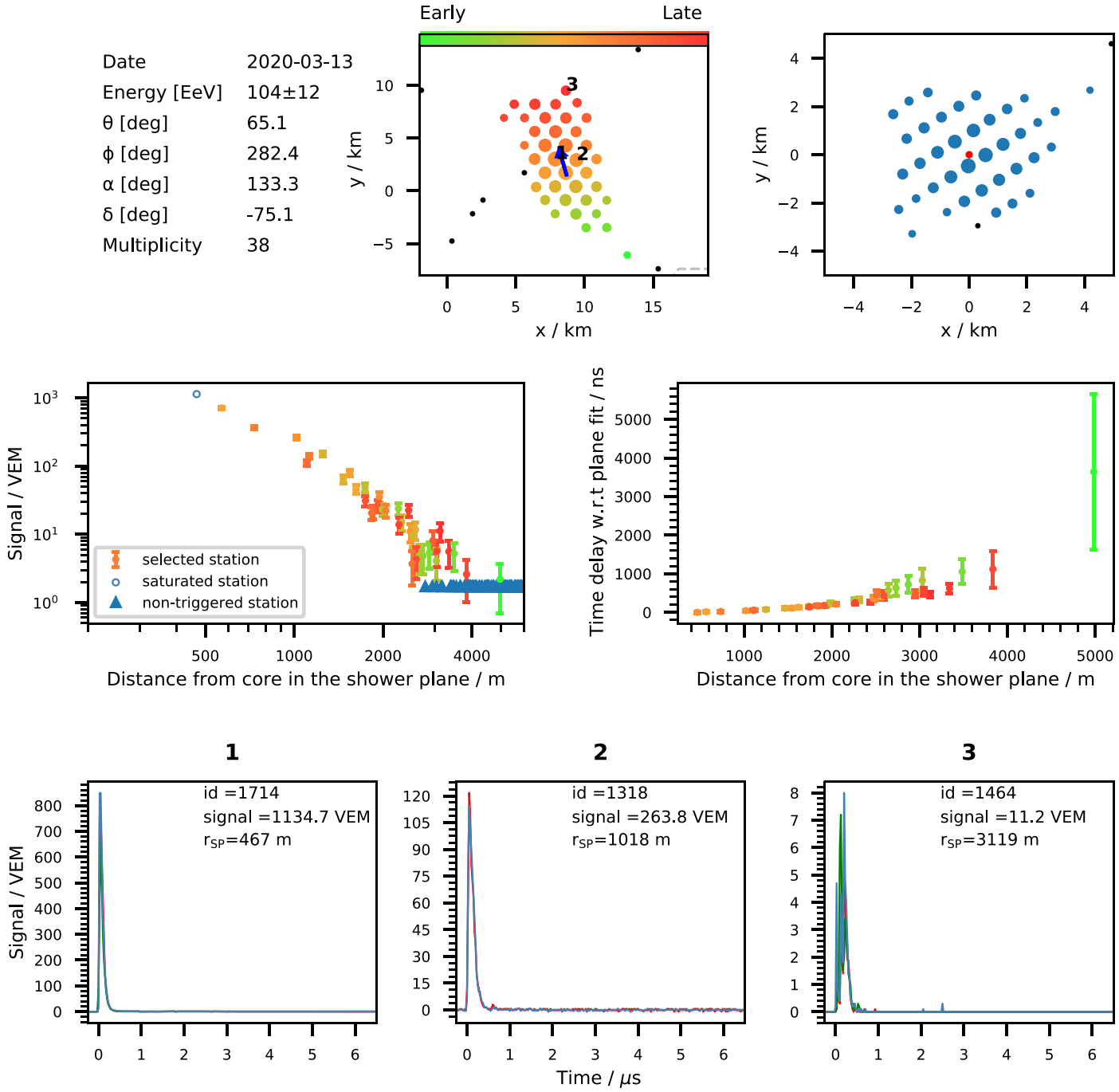

Figure 9. Features of the second most energetic event (PAO200330, #30) belonging to the set of inclined showers ($\theta > 60°$). See text for details.

VEM, a factor of 2.6 greater than the value for the signal in event PAO191110 recorded at a similar distance, 924 m, from the core. As the distance traveled through the atmosphere is substantially shorter for this near-vertical event, the particles suffer less attenuation, resulting in a larger contribution to the signal from the electromagnetic component. This is reflected in the slower risetime: $t_{1/2}(1000) = (360 \pm 10)$ ns. Likewise, a β value of -2.6 indicates that the LDF of this event is steeper than that of event PAO191110, for which β is -2.0.

PAO171228 (#8). An event with primary energy (132 ± 11) EeV arriving with zenith angle $\theta = 41.^{\circ}7$ is shown in Figure 5. As can be seen in the top middle panel, only 19 WCDs have been triggered because the footprint of this event extends beyond the limits of the array (the dashed gray line marks the perimeter). Although the event is not fully contained, the reconstruction of the main observables used in the various physics analyses (Section 3.2) is of high quality.

In the bottom right panel (station ID #1346) there is a signal of over 3 VEM at about 6 μs. Such signals are due to a

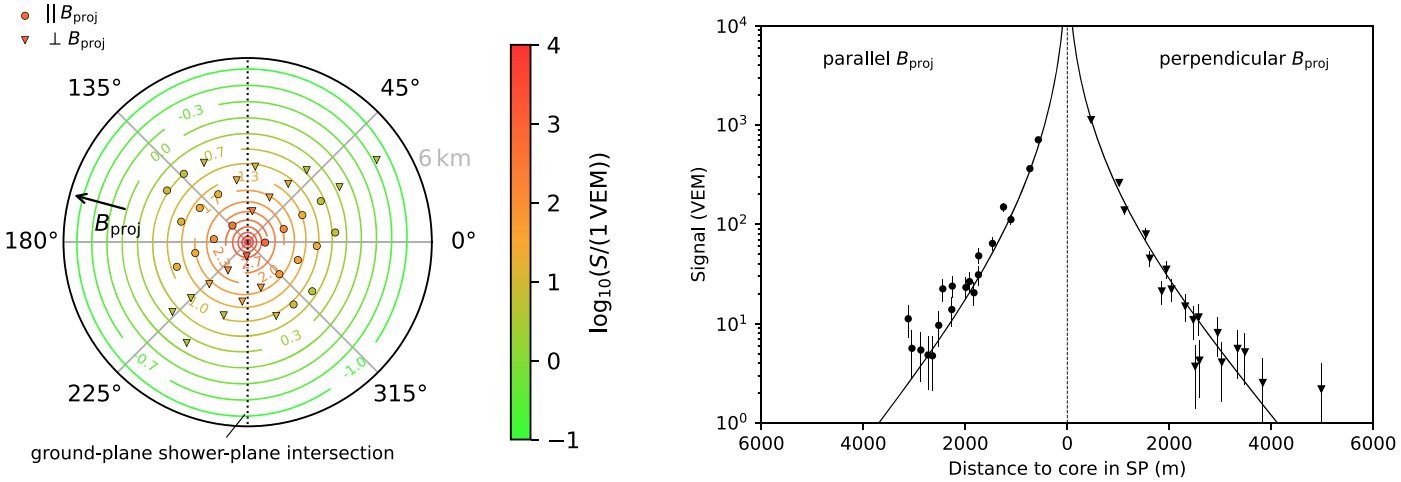

Figure 10. Left: 2D distribution of measured and expected signals in the shower plane. Right: The projection of the signal distribution onto the distance from the shower core. Note the slight asymmetry between the left (late stations) and right (early stations) halves of the signal in the shower plane (left panel) and the lack of asymmetry between stations parallel and perpendicular to the magnetic field (right panel).

contribution from direct light reaching one photomultiplier and are likely caused by the passage of a particle close to the location of the photomultiplier, perhaps moving in an upward direction, or possibly due to light from an electron produced in a muon decay where the decay electron has been emitted toward the photomultiplier. Under these conditions, the Cherenkov photons are detected directly, and a sharp, distinctive signal is recorded by a single photomultiplier, rather than the broader signals produced when the light is scattered on the inner reflective walls of the WCDs. The increase in signal size caused by the direct light varies with distance and is typically about 1% at 1000 m for events arriving close to the vertical.

PAO110127 (#15). This event (Figure 6) has been selected to show some singular signals that are relatively rare. In this event 14 WCDs are triggered and used to measure the energy, (116 ± 9) EeV; zenith angle θ, 24°.9; and risetime at 1000 m, (320 ± 10) ns. However, the detector closest to the core (located at just over 500 m) shows a saturated signal (see the bottom left panel in the figure). In this case, the saturation is due to the overflow of the finite dynamic range of the readout electronics. The procedure used to recover the majority of such signals is discussed in Section 3.2.2 above.

The bottom right panel (station ID #1346) again exemplifies, as in Figure 5, a signal of over 10 VEM at about 3.8 μs that contains a contribution from direct light reaching one photomultiplier.

4.1.2. Inclined Events

PAO150926 (#17). The inclined event, zenith angle $\theta = 77^{\circ}.2$, with the highest energy, (113 ± 14) EeV, is shown in Figure 7. The shower triggered 75 WCDs in an elongated pattern on the ground, over an area close to $(35 \times 6)\,\mathrm{km}^2$. The shower particles must traverse long distances to reach the ground at such inclinations. Thus, electromagnetic particles are mostly absorbed in the atmosphere and the signals at the ground are produced almost entirely by muons. In contrast to those of events with lower inclinations, most of the signal arrives within a very short time of around 200 ns, independently of the location within the shower footprint (see bottom row in Figure 7). Likewise, the distribution of the integrated signal on the ground loses the near-rotational symmetry of more vertical events (Section 3.2.1). Hence, the distribution of the recorded signals as a function of the distance to the shower core shown in the left middle panel cannot be described by a single rotationally symmetric function. In the middle right panel, the delay of the start of the signal in each triggered WCD with respect to a plane shower front is presented. The shower is very asymmetric and cannot be well described by, for example, a concentrically inflated spherical model.

The reconstruction, using a 2D pattern of muon densities at the ground (Section 3.2.3) for this event, is presented in Figure 8. In the left panel, the distribution of the triggered stations around the shower core in the plane perpendicular to the shower direction (the shower plane) is shown in polar coordinates. The coordinate system is such that the y-axis coincides with the intersection of the ground plane with the shower plane (dashed line). Polar angles close to zero (along the positive x-axis) correspond to stations triggering before the shower core arrives at the ground (so-called "early stations"), while angles toward 180° correspond to "late stations." The colored contour lines indicate the expected signals for the distribution of muon densities that best fit the observed signals. The direction of the component of Earth's magnetic field in the shower plane is indicated by the black arrow. Note how the signal pattern is distorted in the direction perpendicular to the magnetic field. In addition to the distortion induced by the geomagnetic field, there is a small difference between the signals of early (right of dashed line) and late stations (left of dashed line). This difference arises from the attenuation of muons, and also from the different angles of incidence of muons on the detectors. In the right-hand panel slices of the LDF parallel and perpendicular to the projected magnetic field are shown.

PAO200313 (#30). This event (Figure 9) is the second-highest-energy inclined event with an energy of (104 ± 12) EeV. At a zenith angle of $\theta = 65^{\circ}.1$, this shower triggered 38 detector stations in an elongated pattern on the ground within $(19 \times 6)\,\mathrm{km}^2$. As in the previous case, the shower pattern at the ground shows some asymmetry. Even at this inclination, there is a substantial electromagnetic component and the additional 3 km of atmosphere (the early–late effect) corresponds to more than five radiation lengths. Thus, the asymmetry arises predominantly from the difference in the

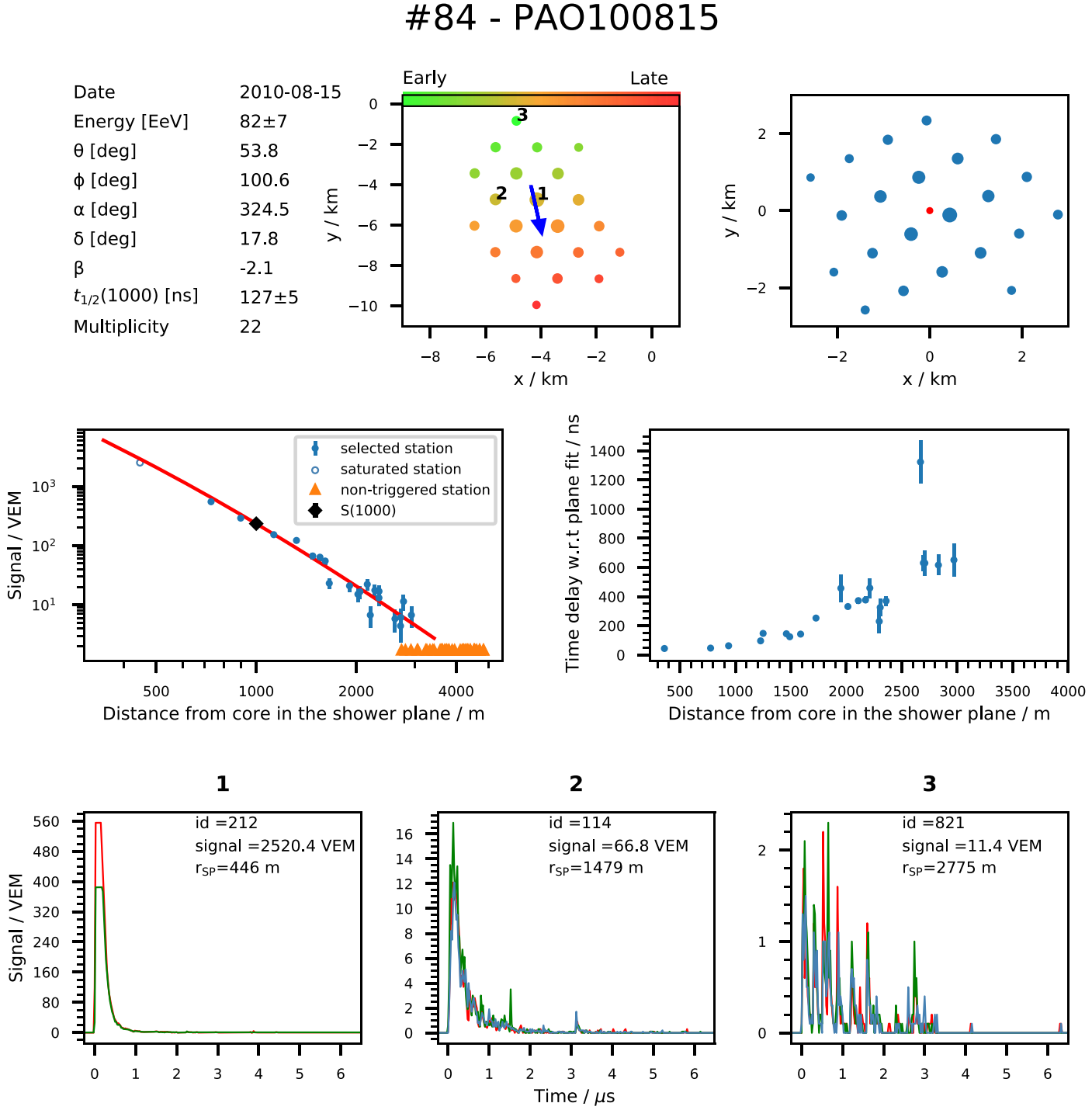

Figure 11. Features of the most energetic hybrid event, PAO100815, #84. See text for details.

attenuation of the electromagnetic component rather than from deflections of the muons in the geomagnetic field. The effect is illustrated in Figure 10.

4.1.3. Hybrid Events

The first of the two events discussed here passes the high-quality criteria applied to select the subsample of hybrid events used for energy calibration (Section 3.3) of vertical events. The second event represents the most energetic shower used in the calibration of inclined events. The details of the 10 most energetic hybrid events used for calibration, including those described below, can be found at https://opendata.auger.org/catalog/.

PAO100815 (#84). This is the most energetic hybrid event, arriving at a zenith angle $\theta = 53^{\circ}.8$. Details of the event are shown in Figures 11–14. The energy estimate from the determination of $S(1000)$ is (82 ± 7) EeV, consistent with the estimate from the fluorescence measurements of (85 ± 4) EeV. There are 22 triggered stations with a footprint of about (7.5×6) km^2. The lateral distribution of signals is described by the modified NKG function. The signals registered by the

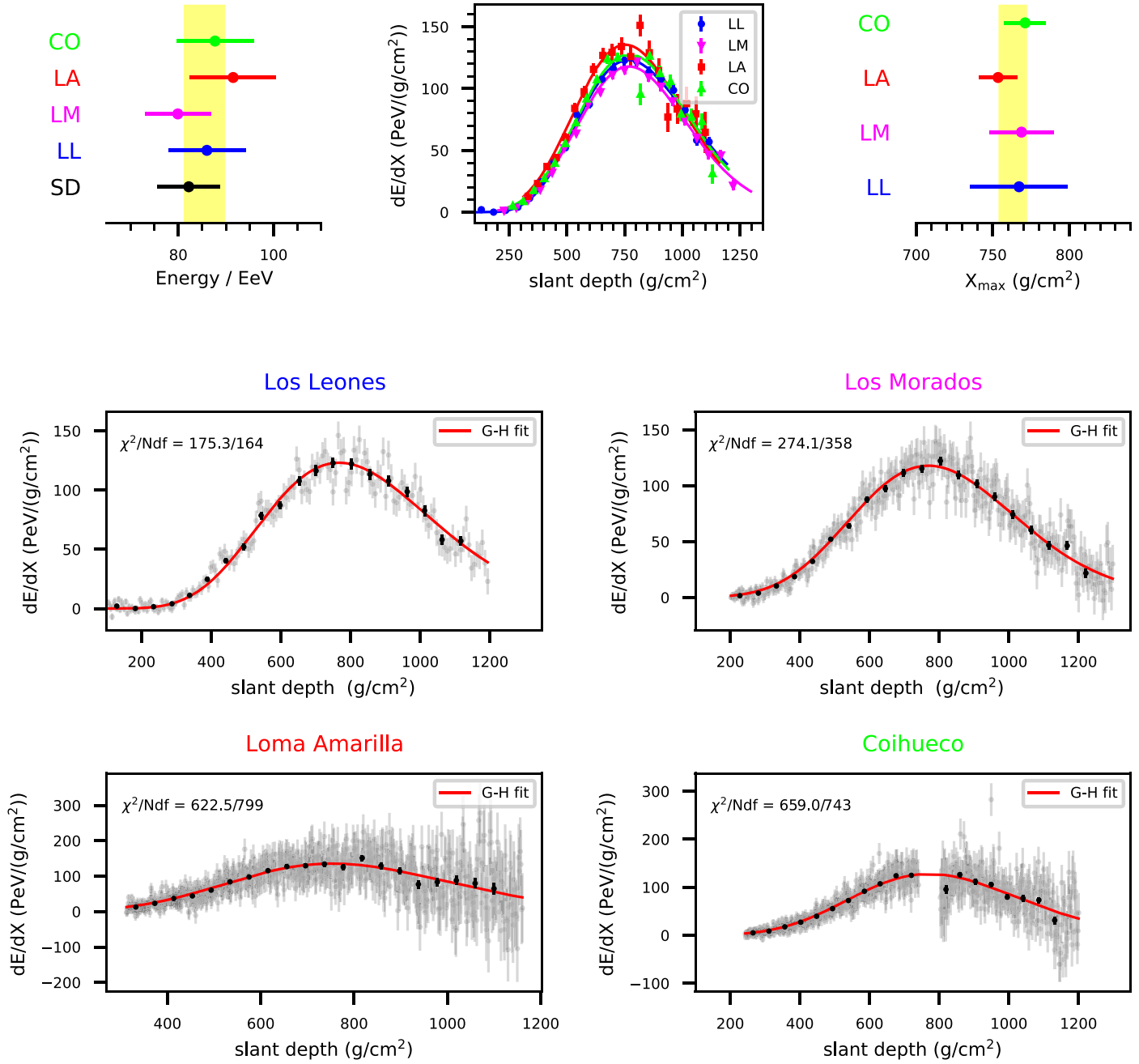

Figure 12. Reconstructed parameters of PAO100815, #84. The FD stations used in the reconstruction are distinguished by different colors. The red lines correspond to fits to the profiles of the energy deposition using the universal shower profile function (Section 3.2.4). The yellow bands are centered on the combined weighted average of the measurements of X_{max} and the energy at the FD sites. The widths of the bands correspond to the statistical uncertainties of combinations. The uncertainty in the SD energy is 8% (Section 3.3).

WCDs are shown in the bottom panels of Figure 11. The light received at the station about 450 m from the shower core (left panel) has saturated the dynamic range of the two photomultipliers (see Section 3.3 and event PAO110127, #15, above) that were operational. The amplitude difference indicates the complexity of the saturation process. For the two detectors with distances to the core larger than 1000 m, the FADCs show the typical structure of shower signals, where the early parts of the FADC traces are dominated by muons and the tails are populated with broader signals due to photons, electrons, and positrons. The risetime at 1000 m is (127 ± 5) ns.

Fluorescence light is detected at all four FD stations. Each individual hybrid reconstruction passes the selection criteria. The reconstructed profiles of the energy deposition in the atmosphere are shown in the lower part of Figure 12, while the reconstructed energies (Section 3.3) and depths of shower maximum (X_{max}) are displayed in the upper section of the figure.

Shower events crossing the field of view of a telescope at larger distances have lower angular velocities than those that pass close to the telescope. Additionally, when a shower is observed to approach the telescope, the signals are registered more rapidly across the camera than those from showers moving away from it. These effects result in different angular velocities of the shower images on the telescope cameras. Accordingly, the number of points is different in the profiles of

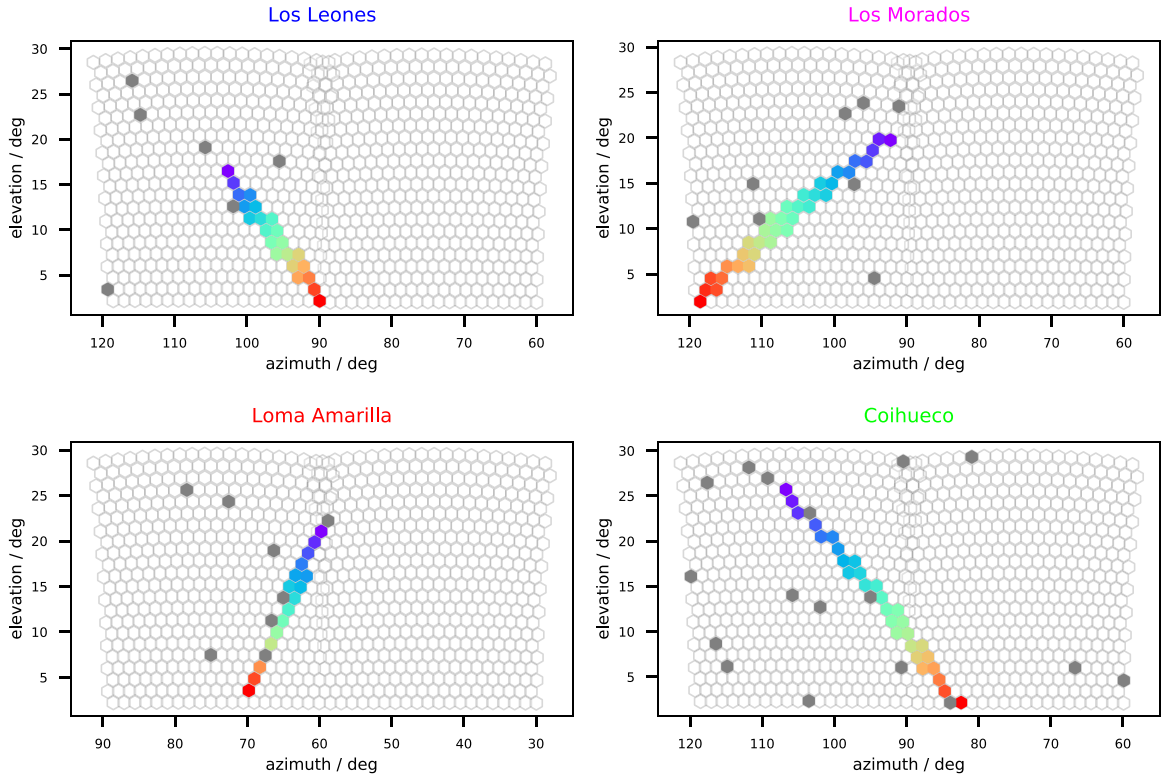

Figure 13. The camera views in all four telescopes for event PAO100815, #84. The colors (violet to red) indicate the times (early to late) at which the light reaches each pixel. Dark pixels are random coincidences and are not used in the reconstruction.

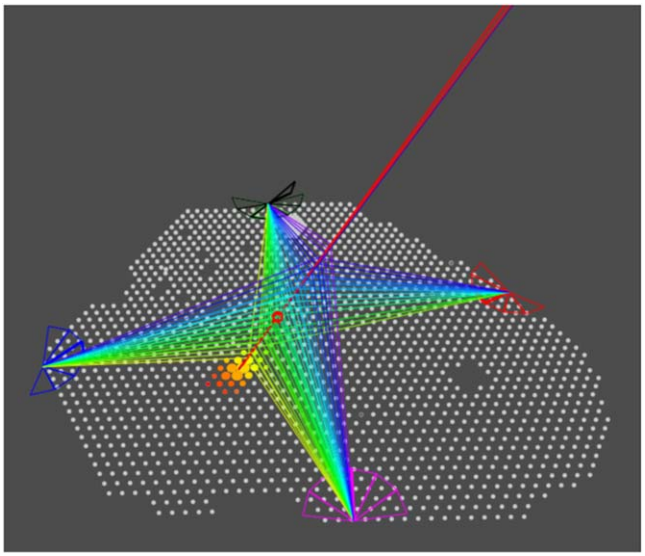

Figure 14. 3D visualization of PAO100815, #84. The lines correspond to the light rays and point to the telescopes of the FDs. The colors of the light rays and of the SD stations represent the trigger times of the FD and SD PMTs, respectively.

the energy deposit recorded at the individual stations. The discrete binning of the energy deposits is a consequence of the 100 ns readout of the photomultipliers of the fluorescence telescopes.

The uncertainties in the energy and $X_{\max}$ estimates from the individual stations of the FD differ mainly because different amounts of Cherenkov light are detected at them. The relatively larger fraction of Cherenkov light (12%) at the Los Leones station results in a larger uncertainty in the longitudinal profile because Cherenkov emission is strongly beamed around the shower axis. Thus, a small uncertainty in the shower geometry translates into a larger uncertainty in this profile when compared with the estimate from Coihueco, where the Cherenkov light is only 5% of the integral of the light flux. The uncertainty is also affected by other effects, such as the distance of the shower to the FD sites, that result in different numbers of photons being detected. At the Coihueco site, the shower image is detected at two telescopes, giving rise to a gap in the reconstruction of the profile of deposited energy. This occurs because the times for which the shower image is close to the border of the field of view of a telescope are rejected as it is not possible to make an accurate estimate of the light flux. Overall, the $X_{\max}$ and energy estimates from the individual FD stations agree within quoted statistical uncertainties.

In Figure 13, the camera views are shown for all eight telescopes at the four sites where the event is detected. The colors assigned to individual pixels represent the centroids of pulses in the photomultipliers, thus marking the arrival time of fluorescence and Cherenkov light at the telescopes. Dark gray pixels indicate pixels that are triggered randomly that do not match the time fit used to determine the shower geometry (Section 3.2.4). These random triggers arise from the night-sky background, which varies for each detected shower and with the direction in which a telescope is pointing. There are no such pixels in the telescopes shown for event PAO140131, #101 (Figure 16). The horizontal axes in the camera views correspond to local azimuth angles, defined counterclockwise from the back wall of the FD station. The origin points to the right, looking on to the shower from the position of the station. The vertical axis is an angular elevation of the viewing direction of the FD pixels.

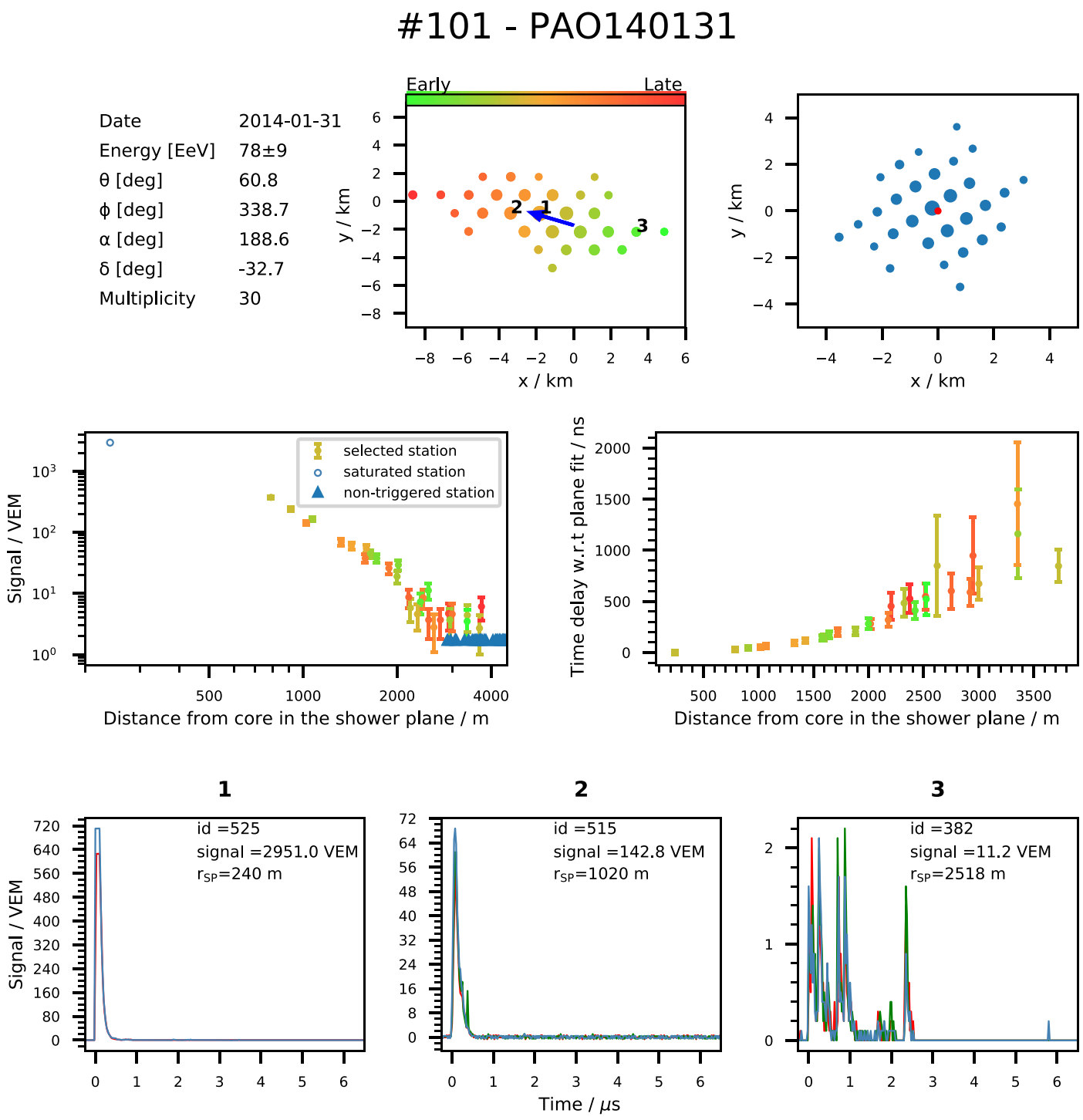

Figure 15. The parameters reconstructed using the data from the WCDs for event PAO140131, #101.

In Figure 14 a 3D view of the event is exhibited.

PAO140131 (#101). This is the second most energetic hybrid event and belongs to the data set used to calibrate events with zenith angles above 60°. The zenith angle $\theta = 60.^{\circ}8$. The energy reconstructed from the SD signals is (78 ± 9) EeV, consistent with the energy from the fluorescence measurement of (73 ± 8) EeV. With 30 triggered stations, the footprint is elongated and covers an area of (14×6) km^2. At 60°, the depth of the atmosphere is twice the atmospheric vertical depth. Thus the electromagnetic component of the shower is partially quenched (see Section 3.2.2). The LDF and the time delay of the start time signals are barely asymmetric (see Figure 15) and can thus be described by the modified NKG function used for the vertical reconstruction.

Fluorescence light is detected at three FD stations (Los Morados, Coihueco, and Loma Amarilla), but only the reconstruction for Loma Amarilla passes the selection criteria. The profile of energy deposition (Figure 16, bottom right) is obtained from the profile of the detected light (Figure 16, bottom left). The color bands in the figure of the light flux

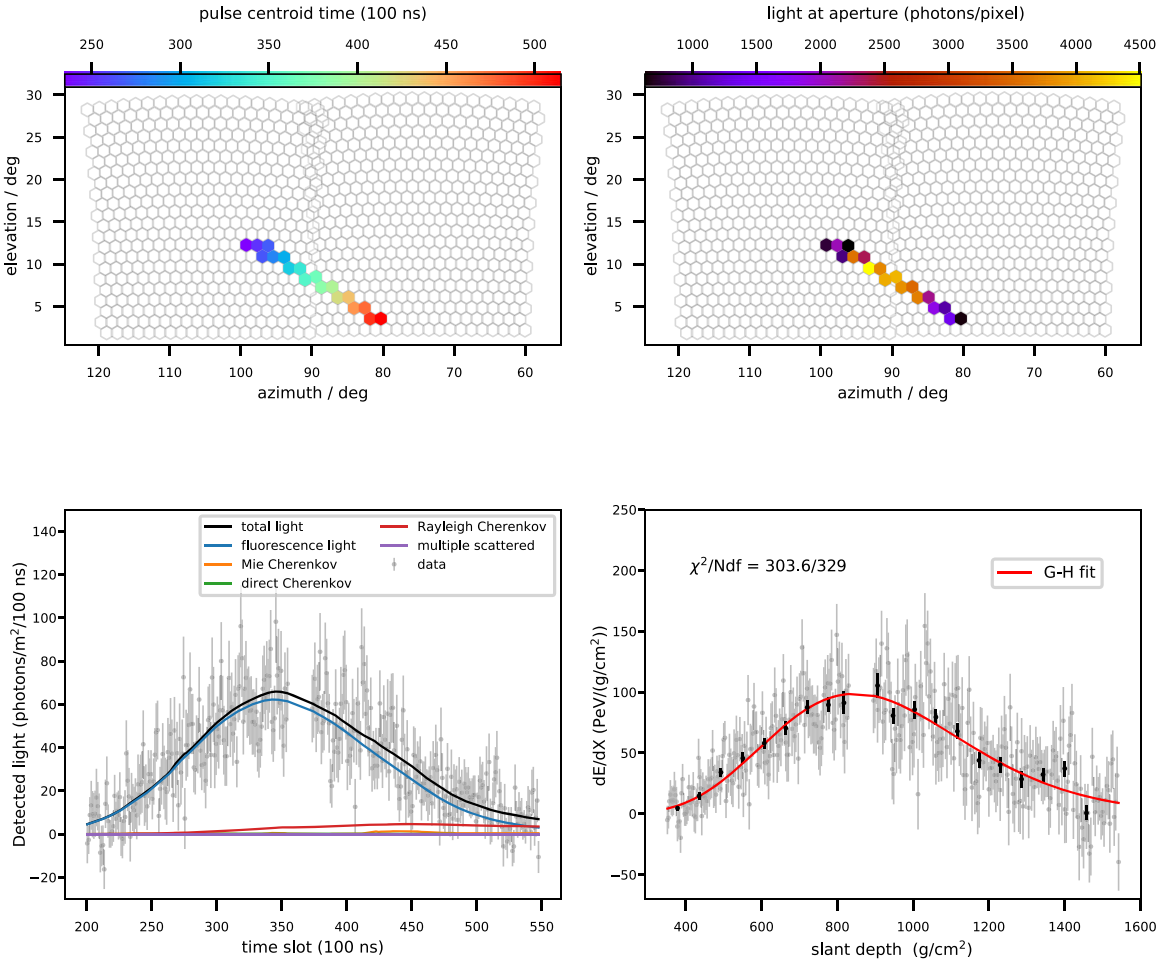

Figure 16. Data from the fluorescence telescopes in event PAO140131 (#101). The profile of the energy deposits (bottom right) is accompanied by the light flux profile (bottom left) and the camera views from two telescopes at Loma Amarilla (top). The shower fell far from the telescopes with the closest point to the shower axis being about 35 km.

profile show the contributions from different light sources. Fluorescence light dominates, while Cherenkov light scattered into the telescope makes up 10% of the integrated signal.

The top panels of Figure 16 show the camera views of the shower crossing two adjacent telescopes at the Loma Amarilla site. The photomultipliers are sequentially triggered (top left panel with colors coding the trigger time). The charges at each photomultiplier are proportional to the light flux received at the entrance window of each telescope. The shower image is detected in two telescopes giving rise to a gap in the reconstruction of the profile.

5. A Sky Map of the 100 Highest-energy Events

A map showing the R.A. and decl. of the 100 highest-energy events is displayed in Figure 17.

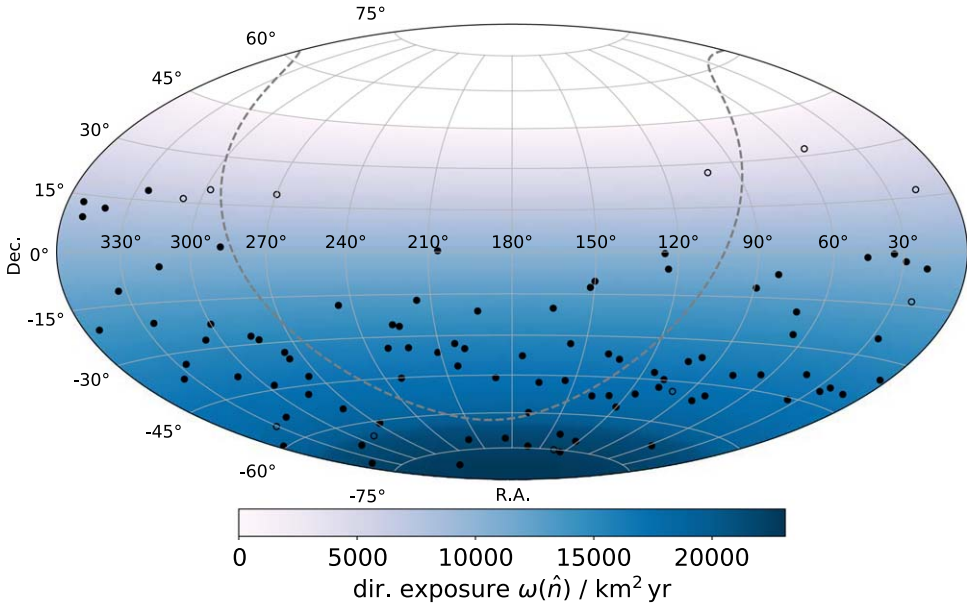

Figure 17. The positions of the arrival directions of the 100 highest-energy cosmic rays detected at the Pierre Auger Observatory shown in equatorial coordinates. The open circles show the arrival directions of the inclined events. The graded color scale shows how the exposure varies with decl. for the whole data set. The white region, above ∼45°, is not accessible from the latitude of Malargüe. The dashed line indicates the Galactic plane.

The successful installation, commissioning, and operation of the Pierre Auger Observatory would not have been possible without the strong commitment and effort from the technical and administrative staff in Malargüe. We are very grateful to the following agencies and organizations for their financial support:

(Argentina) Comisión Nacional de Energía Atómica; Agencia Nacional de Promoción Científica y Tecnológica (ANPCyT); Consejo Nacional de Investigaciones Científicas y Técnicas (CONICET); Gobierno de la Provincia de Mendoza; Municipalidad de Malargüe; NDM Holdings and Valle Las Leñas (in gratitude for their continuing cooperation over land access); (Australia) the Australian Research Council; (Belgium) Fonds de la Recherche Scientifique (FNRS); Research Foundation Flanders (FWO); (Brazil) Conselho Nacional de Desenvolvimento Científico e Tecnológico (CNPq); Financiadora de Estudos e Projetos (FINEP); Fundação de Amparo à Pesquisa do Estado de Rio de Janeiro (FAPERJ); São Paulo Research Foundation (FAPESP) grant Nos. 2019/10151-2, 2010/07359-6, and 1999/05404-3; Ministério da Ciência, Tecnologia, Inovações e Comunicações (MCTIC); (Czech Republic) grant Nos. MSMT CR LTT18004, LM2015038, LM2018102, CZ.02.1.01/0.0/0.0/16_013/0001402, CZ.02.1.01/0.0/0.0/18_046/0016010, and CZ.02.1.01/0.0/0.0/17_049/0008422; (France) Centre de Calcul IN2P3/CNRS; Centre National de la Recherche Scientifique (CNRS); Conseil Régional Ile-de-France; Département Physique Nucléaire et Corpusculaire (PNC-IN2P3/CNRS); Département Sciences de l'Univers (SDU-INSU/CNRS); Institut Lagrange de Paris grant No. LABEX ANR-10-LABX-63 within the Investissements d'Avenir program, grant No. ANR-11-IDEX-0004-02; (Germany) Bundesministerium für Bildung und Forschung (BMBF); Deutsche Forschungsgemeinschaft; Finanzministerium Baden-Württemberg; Helmholtz Alliance for Astroparticle Physics; Helmholtz-Gemeinschaft Deutscher Forschungszentren; Ministerium für Kultur und Wissenschaft des Landes Nordrhein-Westfalen; Ministerium für Wissenschaft, Forschung und Kunst des Landes Baden-Württemberg; (Italy) Istituto Nazionale di Fisica Nucleare (INFN); Istituto Nazionale di Astrofisica (INAF); Ministero dell'Istruzione, dell'Universitá e della Ricerca (MIUR); CETEMPS Center of Excellence; Ministero degli Affari Esteri; (Mexico) Consejo Nacional de Ciencia y Tecnología (CONACYT) No. 167733; Universidad Nacional Autónoma de México (UNAM); PAPIIT DGAPA-UNAM; (The Netherlands) Ministry of Education, Culture and Science; Netherlands Organisation for Scientific Research (NWO); Dutch national e-infrastructure with the support of SURF Cooperative; (Poland) Ministry of Education and Science, grant No. DIR/WK/2018/11; National Science Centre, grant Nos. 2016/22/M/ST9/00198, 2016/23/B/ST9/01635, and 2020/39/B/ST9/01398; (Portugal) Portuguese national funds and FEDER funds within Programa Operacional Factores de Competitividade through Fundação para a Ciência e a Tecnologia (COMPETE); (Romania) Ministry of Research, Innovation and Digitization, CNCS/CCCDI UEFISCDI, grant Nos. PN19150201/16N/2019 and PN1906010 within the National Nucleus Program, and project Nos. TE128, PN-III-P1-1.1-TE-2021-0924/TE57/2022, and PED289, within PNCDI III; (Slovenia) Slovenian Research Agency, grants P1-0031, P1-0385, I0-0033, and N1-0111; (Spain) Ministerio de Economía, Industria y Competitividad (FPA2017-85114-P and PID2019-104676GB-C32); Xunta de Galicia (ED431C 2017/07); Junta de Andalucía (SOMM17/6104/UGR, P18-FR-4314); Feder Funds; RENATA / Red Nacional Temática de Astropartículas (FPA2015-68783-REDT); María de Maeztu Unit of Excellence (MDM-2016-0692); (USA) Department of Energy, contract Nos. DE-AC02-07CH11359, DE-FR02-04ER41300, DE-FG02-99ER41107, and DE-SC0011689; National Science Foundation, grant No. 0450696; the Grainger Foundation; Marie Curie-IRSES/EPLANET; the European Particle Physics Latin American Network; and UNESCO.

ORCID iDs

A. Abdul Halim https://orcid.org/0000-0003-1218-1737
P. Abreu https://orcid.org/0000-0002-9973-7314
M. Aglietta https://orcid.org/0000-0001-8354-5388

I. Allekotte https://orcid.org/0000-0002-9624-3044
K. Almeida Cheminant https://orcid.org/0000-0001-6352-5339
A. Almela https://orcid.org/0000-0003-1233-2670
J. Alvarez-Muñiz https://orcid.org/0000-0002-2367-0803
J. Ammerman Yebra https://orcid.org/0000-0002-2059-6206
G. A. Anastasi https://orcid.org/0000-0003-0824-5283
L. Anchordoqui https://orcid.org/0000-0003-1463-7136
S. Andringa https://orcid.org/0000-0002-6397-9207
C. Aramo https://orcid.org/0000-0002-8412-3846
P. R. Araújo Ferreira https://orcid.org/0000-0002-0502-3602
E. Arnone https://orcid.org/0000-0001-6740-5051
H. Asorey https://orcid.org/0000-0002-4559-8785
P. Assis https://orcid.org/0000-0001-7765-3606
E. Avocone https://orcid.org/0000-0003-3757-2718
A. M. Badescu https://orcid.org/0000-0001-6510-4124
A. Bakalova https://orcid.org/0000-0003-1001-4484
A. Balaceanu https://orcid.org/0000-0001-7639-1253
F. Barbato https://orcid.org/0000-0003-0751-6731
J. A. Bellido https://orcid.org/0000-0002-0833-9194
C. Berat https://orcid.org/0000-0001-8294-6294
M. E. Bertaina https://orcid.org/0000-0003-1069-1397
G. Bhatta https://orcid.org/0000-0002-0705-6619
P. L. Biermann https://orcid.org/0000-0003-3948-6143
K. Bismark https://orcid.org/0000-0001-8637-7041
T. Bister https://orcid.org/0000-0003-4005-0857
J. Biteau https://orcid.org/0000-0002-4202-8939
J. Blazek https://orcid.org/0000-0002-5870-8947
C. Bleve https://orcid.org/0000-0001-6841-3280
J. Blümer https://orcid.org/0000-0001-7715-9608
M. Boháčová https://orcid.org/0000-0001-6014-723X
D. Boncioli https://orcid.org/0000-0003-1186-9353
C. Bonifazi https://orcid.org/0000-0002-3087-3609
L. Bonneau Arbeletche https://orcid.org/0000-0003-4544-9808
N. Borodai https://orcid.org/0000-0003-1864-937X
J. Brack https://orcid.org/0000-0003-4096-2063
A. Bueno https://orcid.org/0000-0002-7439-4247
S. Buitink https://orcid.org/0000-0002-6177-497X
M. Buscemi https://orcid.org/0000-0003-2123-5434
M. Büsken https://orcid.org/0000-0002-2174-5779
A. Bwembya https://orcid.org/0000-0002-6995-5978
K. S. Caballero-Mora https://orcid.org/0000-0002-4042-3855
L. Caccianiga https://orcid.org/0000-0002-2245-5108
R. Caruso https://orcid.org/0000-0003-1622-8731
A. Castellina https://orcid.org/0000-0002-0045-2467
F. Catalani https://orcid.org/0000-0001-9332-1476
G. Cataldi https://orcid.org/0000-0001-8066-7718
L. Cazon https://orcid.org/0000-0001-6748-8395
J. A. Chinellato https://orcid.org/0000-0002-3240-6270
J. Chudoba https://orcid.org/0000-0002-6425-2579
L. Chytka https://orcid.org/0000-0001-5741-259X
R. W. Clay https://orcid.org/0000-0002-9040-9648
A. C. Cobos Cerutti https://orcid.org/0000-0002-0652-5460
R. Colalillo https://orcid.org/0000-0002-4179-9352
A. Coleman https://orcid.org/0000-0003-1510-1712
M. R. Coluccia https://orcid.org/0000-0002-3023-0566
R. Conceição https://orcid.org/0000-0003-4945-5340
A. Condorelli https://orcid.org/0000-0001-5681-0086
G. Consolati https://orcid.org/0000-0003-3614-245X
F. Convenga https://orcid.org/0000-0002-2841-1034
D. Correia dos Santos https://orcid.org/0000-0001-8243-6710
C. E. Covault https://orcid.org/0000-0001-5405-5371
M. Cristinziani https://orcid.org/0000-0003-3893-9171
S. Dasso https://orcid.org/0000-0002-7680-4721
K. Daumiller https://orcid.org/0000-0002-0527-4823
B. R. Dawson https://orcid.org/0000-0002-4271-3055
S. J. de Jong https://orcid.org/0000-0002-3120-3367
J. R. T. de Mello Neto https://orcid.org/0000-0002-3234-6634
I. De Mitri https://orcid.org/0000-0002-8665-1730
F. de Palma https://orcid.org/0000-0001-5898-2834
V. de Souza https://orcid.org/0000-0003-0865-233X
E. De Vito https://orcid.org/0000-0003-2045-7588
A. Del Popolo https://orcid.org/0000-0002-9057-0239
O. Deligny https://orcid.org/0000-0001-6863-6572
A. di Matteo https://orcid.org/0000-0002-8260-1867
M. Dobre https://orcid.org/0000-0003-4032-7318
C. Dobrigkeit https://orcid.org/0000-0002-1236-0789
L. M. Domingues Mendes https://orcid.org/0000-0003-0651-9404
R. C. dos Anjos https://orcid.org/0000-0002-6463-2272
J. Ebr https://orcid.org/0000-0001-8807-6162
M. Eman https://orcid.org/0000-0002-7247-936X
R. Engel https://orcid.org/0000-0003-2924-8889
I. Epicoco https://orcid.org/0000-0002-6408-1335
M. Erdmann https://orcid.org/0000-0002-1653-1303
A. Etchegoyen https://orcid.org/0000-0001-6989-2404
H. Falcke https://orcid.org/0000-0002-2526-6724
G. Farrar https://orcid.org/0000-0003-2417-5975
A. C. Fauth https://orcid.org/0000-0001-7239-0288
F. Fenu https://orcid.org/0000-0002-0313-8852
J. M. Figueira https://orcid.org/0000-0002-6768-5214
A. Filipčič https://orcid.org/0000-0001-5671-1555
T. Fitoussi https://orcid.org/0000-0001-9473-9356
T. Fujii https://orcid.org/0000-0003-2401-504X
A. Fuster https://orcid.org/0000-0002-6575-7958
C. Galea https://orcid.org/0000-0002-3075-6605
C. Galelli https://orcid.org/0000-0002-7372-9703
B. García https://orcid.org/0000-0003-0919-2734
F. Gesualdi https://orcid.org/0000-0002-4080-7840
A. Gherghel-Lascu https://orcid.org/0000-0002-8757-2081
P. L. Ghia https://orcid.org/0000-0003-1101-4857
J. Glombitza https://orcid.org/0000-0001-9683-4568
F. Gollan https://orcid.org/0000-0002-0495-2768
G. Golup https://orcid.org/0000-0001-9471-8811
M. Gómez Berisso https://orcid.org/0000-0001-5530-0180
P. F. Gómez Vitale https://orcid.org/0000-0001-9689-2020
J. M. González https://orcid.org/0000-0003-3003-5063
N. González https://orcid.org/0000-0001-6566-2222
D. Góra https://orcid.org/0000-0002-4853-5974
A. Gorgi https://orcid.org/0000-0002-8085-2304
F. Guarino https://orcid.org/0000-0003-1427-9885
E. Guido https://orcid.org/0000-0002-0772-7654
P. Hamal https://orcid.org/0000-0003-3139-7234
M. R. Hampel https://orcid.org/0000-0001-7622-4826
P. Hansen https://orcid.org/0000-0001-7015-2374
D. Harari https://orcid.org/0000-0002-7350-2488
V. M. Harvey https://orcid.org/0000-0001-9090-8415
A. Haungs https://orcid.org/0000-0002-9638-7574

T. Hebbeker https://orcid.org/0000-0002-9736-266X
C. Hojvat https://orcid.org/0000-0003-3323-3129
J. R. Hörandel https://orcid.org/0000-0001-6604-547X
P. Horvath https://orcid.org/0000-0002-6710-5339
M. Hrabovský https://orcid.org/0000-0003-4223-7316
T. Huege https://orcid.org/0000-0002-2783-4772
A. Insolia https://orcid.org/0000-0002-9040-1566
P. G. Isar https://orcid.org/0000-0002-1241-584X
P. Janecek https://orcid.org/0000-0003-3501-7163
J. Jurysek https://orcid.org/0000-0002-3130-4168
A. Kääpä https://orcid.org/0000-0002-2410-4491
K. H. Kampert https://orcid.org/0000-0002-2805-0195
B. Keilhauer https://orcid.org/0000-0003-4494-1155
A. Khakurdikar https://orcid.org/0000-0002-4857-5255
V. V. Kizakke Covilakam https://orcid.org/0000-0001-5278-3172
H. O. Klages https://orcid.org/0000-0002-4306-021X
M. Kleifges https://orcid.org/0000-0002-7608-4058
B. L. Lago https://orcid.org/0000-0001-9672-0499
N. Langner https://orcid.org/0000-0001-7443-3042
V. Lenok https://orcid.org/0000-0002-7921-2035
A. Letessier-Selvon https://orcid.org/0000-0002-2044-3103
I. Lhenry-Yvon https://orcid.org/0000-0002-7887-3288
D. Lo Presti https://orcid.org/0000-0002-4540-2885
L. Lopes https://orcid.org/0000-0001-8571-0033
L. Lu https://orcid.org/0000-0003-3175-7770
Q. Luce https://orcid.org/0000-0003-3745-6709
J. P. Lundquist https://orcid.org/0000-0002-4245-5092
A. Machado Payeras https://orcid.org/0000-0001-7635-4348
D. Mandat https://orcid.org/0000-0001-7748-7468
P. Mantsch https://orcid.org/0000-0002-8382-7745
S. Marafico https://orcid.org/0000-0003-4604-4677
F. M. Mariani https://orcid.org/0000-0002-1683-1162
A. G. Mariazzi https://orcid.org/0000-0002-9876-2470
I. C. Mariş https://orcid.org/0000-0002-5771-1124
G. Marsella https://orcid.org/0000-0002-3152-8874
D. Martello https://orcid.org/0000-0003-2046-3910
O. Martínez Bravo https://orcid.org/0000-0001-9052-856X
M. A. Martins https://orcid.org/0000-0002-7294-6204
H. J. Mathes https://orcid.org/0000-0002-0680-040X
J. Matthews https://orcid.org/0000-0002-1832-4420
G. Matthiae https://orcid.org/0000-0003-3036-2590
E. Mayotte https://orcid.org/0000-0003-2618-9166
S. Mayotte https://orcid.org/0000-0001-8957-8033
P. O. Mazur https://orcid.org/0000-0003-4076-6732
G. Medina-Tanco https://orcid.org/0000-0002-3202-319X
L. Miramonti https://orcid.org/0000-0002-2808-5363
S. Mollerach https://orcid.org/0000-0002-9339-5317
F. Montanet https://orcid.org/0000-0001-9787-596X
L. Morejon https://orcid.org/0000-0003-1494-2624
A. L. Müller https://orcid.org/0000-0002-8473-695X
K. Mulrey https://orcid.org/0000-0001-8026-8020
R. Mussa https://orcid.org/0000-0002-0294-9071
M. Muzio https://orcid.org/0000-0003-4615-5529
L. Nellen https://orcid.org/0000-0003-1059-8731
G. Nicora https://orcid.org/0000-0001-7504-6423
M. Niechciol https://orcid.org/0000-0001-6823-8056
D. Nitz https://orcid.org/0000-0001-5538-9867
D. Nosek https://orcid.org/0000-0001-6219-200X
V. Novotny https://orcid.org/0000-0002-4319-4541
L. Nožka https://orcid.org/0000-0002-8774-7099
A Nucita https://orcid.org/0000-0002-7926-3481
L. A. Núñez https://orcid.org/0000-0003-4575-5899
M. Palatka https://orcid.org/0000-0003-2061-6059
J. Pallotta https://orcid.org/0000-0003-4846-8748
G. Parente https://orcid.org/0000-0003-2847-0461
M. Pech https://orcid.org/0000-0002-8421-0456
J. Pękala https://orcid.org/0000-0002-1062-5595
R. Pelayo https://orcid.org/0000-0001-6973-1731
E. E. Pereira Martins https://orcid.org/0000-0002-1167-8314
C. Pérez Bertolli https://orcid.org/0000-0002-9790-5732
L. Perrone https://orcid.org/0000-0002-8150-4336
S. Petrera https://orcid.org/0000-0002-6029-1255
C. Petrucci https://orcid.org/0000-0003-3751-581X
T. Pierog https://orcid.org/0000-0002-7472-8710
M. Pimenta https://orcid.org/0000-0002-2590-0908
M. Platino https://orcid.org/0000-0001-6644-7970
B. Pont https://orcid.org/0000-0002-2578-5364
P. Privitera https://orcid.org/0000-0002-0623-9261
M. Prouza https://orcid.org/0000-0002-3238-9597
A. Puyleart https://orcid.org/0000-0001-5975-9036
S. Querchfeld https://orcid.org/0000-0003-2787-5010
D. Ravignani https://orcid.org/0000-0001-7410-8522
J. Ridky https://orcid.org/0000-0001-6697-1393
F. Riehn https://orcid.org/0000-0001-8434-7500
M. Risse https://orcid.org/0000-0001-9660-8683
V. Rizi https://orcid.org/0000-0002-5277-6527
W. Rodrigues de Carvalho https://orcid.org/0000-0002-2328-7628
M. Roth https://orcid.org/0000-0003-1281-4477
E. Roulet https://orcid.org/0000-0003-1478-9260
A. C. Rovero https://orcid.org/0000-0001-6979-5604
P. Ruehl https://orcid.org/0000-0001-9645-8363
A. Saftoiu https://orcid.org/0000-0002-7903-6510
M. Saharan https://orcid.org/0000-0001-7193-5506
F. Salamida https://orcid.org/0000-0002-9306-8447
H. Salazar https://orcid.org/0000-0003-4556-7302
F. Sánchez https://orcid.org/0000-0002-6861-6261
E. M. Santos https://orcid.org/0000-0002-2818-8813
E. Santos https://orcid.org/0000-0002-0474-8863
F. Sarazin https://orcid.org/0000-0001-5614-1986
R. Sarmento https://orcid.org/0000-0002-5018-5467
P. Savina https://orcid.org/0000-0001-7670-554X
C. M. Schäfer https://orcid.org/0000-0002-4477-9218
V. Scherini https://orcid.org/0000-0003-3762-4063
H. Schieler https://orcid.org/0000-0002-2637-4778
M. Schimassek https://orcid.org/0000-0003-4295-7719
M. Schimp https://orcid.org/0000-0001-6407-7187
F. Schlüter https://orcid.org/0000-0002-5545-4363
D. Schmidt https://orcid.org/0000-0001-6963-1191
O. Scholten https://orcid.org/0000-0003-3649-1254
H. Schoorlemmer https://orcid.org/0000-0002-8999-9249
P. Schovánek https://orcid.org/0000-0002-5344-7645
F. G. Schröder https://orcid.org/0000-0001-8495-7210
J. Schulte https://orcid.org/0000-0002-5822-2445
T. Schulz https://orcid.org/0000-0003-0661-492X
S. J. Sciutto https://orcid.org/0000-0003-1148-3231
M. Scornavacche https://orcid.org/0000-0002-7519-9806
A. Segreto https://orcid.org/0000-0001-7341-6603
S. Sehgal https://orcid.org/0000-0001-5859-7987
G. Sigl https://orcid.org/0000-0002-4396-645X
R. Smau https://orcid.org/0000-0003-3362-3821

R. Šmída https://orcid.org/0000-0003-0122-1123
P. Sommers https://orcid.org/0000-0003-3488-5460
J. F. Soriano https://orcid.org/0000-0002-6253-7378
M. Stadelmaier https://orcid.org/0000-0002-7943-6012
D. Stanca https://orcid.org/0000-0002-8462-2426
S. Stanič https://orcid.org/0000-0003-3344-8381
J. Stasielak https://orcid.org/0000-0002-9284-7000
P. Stassi https://orcid.org/0000-0001-5584-8410
M. Suárez-Durán https://orcid.org/0000-0003-1451-630X
T. Suomijärvi https://orcid.org/0000-0003-1422-258X
A. D. Supanitsky https://orcid.org/0000-0002-6942-6216
Z. Szadkowski https://orcid.org/0000-0002-2690-9912
A. Tapia https://orcid.org/0000-0003-0585-7161
C. Taricco https://orcid.org/0000-0002-0129-5539
C. Timmermans https://orcid.org/0000-0003-4017-2475
O. Tkachenko https://orcid.org/0000-0001-6393-7851
P. Tobiska https://orcid.org/0000-0002-0526-9098
C. J. Todero Peixoto https://orcid.org/0000-0003-3669-8212
B. Tomé https://orcid.org/0000-0002-7564-8392
Z. Torrès https://orcid.org/0000-0002-8327-8459
A. Travaini https://orcid.org/0000-0001-7875-2147
P. Travnicek https://orcid.org/0000-0002-1655-9584
C. Trimarelli https://orcid.org/0000-0002-8811-3266
M. Tueros https://orcid.org/0000-0003-1570-1419
R. Ulrich https://orcid.org/0000-0002-2535-402X
M. Unger https://orcid.org/0000-0002-7651-0272
L. Vaclavek https://orcid.org/0000-0002-0910-3415
M. Vacula https://orcid.org/0000-0003-4844-3962
J. F. Valdés Galicia https://orcid.org/0000-0002-8917-9259
L. Valore https://orcid.org/0000-0003-2682-8378
E. Varela https://orcid.org/0000-0003-0715-7513
A. Vásquez-Ramírez https://orcid.org/0000-0001-7499-9302
D. Veberič https://orcid.org/0000-0003-2683-1526
C. Ventura https://orcid.org/0000-0002-9261-424X
I. D. Vergara Quispe https://orcid.org/0000-0001-8377-5933
V. Verzi https://orcid.org/0000-0003-2291-9387
J. Vicha https://orcid.org/0000-0002-7945-3605
J. Vink https://orcid.org/0000-0002-0816-994
S. Vorobiov https://orcid.org/0000-0001-8679-3424
A. A. Watson https://orcid.org/0000-0002-3727-6786
A. Weindl https://orcid.org/0000-0003-4929-6191
L. Wiencke https://orcid.org/0000-0003-2878-9704
H. Wilczyński https://orcid.org/0000-0003-2652-9685
B. Wundheiler https://orcid.org/0000-0003-3121-7037
A. Yushkov https://orcid.org/0000-0001-5107-9116
O. Zapparrata https://orcid.org/0000-0002-8839-4715
E. Zas https://orcid.org/0000-0002-4430-8117
D. Zavrtanik https://orcid.org/0000-0002-4596-1521
M. Zavrtanik https://orcid.org/0000-0001-5606-6912

References

Aab, A., Abreu, P., Aglietta, M., et al. 2014a, PhRvD, 90, 122005
Aab, A., Abreu, P., Aglietta, M., et al. 2014b, PhRvD, 90, 122006
Aab, A., Abreu, P., Aglietta, M., et al. 2014c, JCAP, 08, 019
Aab, A., Abreu, P., Aglietta, M., et al. 2015a, NIMPA, 798, 172
Aab, A., Abreu, P., Aglietta, M., et al. 2015b, JCAP, 08, 049
Aab, A., Abreu, P., Aglietta, M., et al. 2016, PhRvD, 93, 072006
Aab, A., Abreu, P., Aglietta, M., et al. 2017a, Sci, 357, 1266
Aab, A., Abreu, P., Aglietta, M., et al. 2017b, PhRvD, 96, 122003
Aab, A., Abreu, P., Aglietta, M., et al. 2017c, ApJL, 837, L25
Aab, A., Abreu, P., Aglietta, M., et al. 2017d, JInst, 12, P02006
Aab, A., Abreu, P., Aglietta, M., et al. 2019a, JCAP, 10, 022
Aab, A., Abreu, P., Aglietta, M., et al. 2019b, PhRvD, 100, 082003
Aab, A., Abreu, P., Aglietta, M., et al. 2020a, PhRvD, 102, 062005
Aab, A., Abreu, P., Aglietta, M., et al. 2020b, JInst, 15, P10021
Abraham, J., Abreu, P., Aglietta, M., et al. 2010a, NIMPA, 613, 29
Abraham, J., Abreu, P., Aglietta, M., et al. 2010b, NIMPA, 620, 227
Abreu, P., Aglietta, M., Ahn, E. J., et al. 2011, JCAP, 11, 022
Abreu, P., Aglietta, M., Ahlers, M., et al. 2012, JInst, 7, P09001
Abreu, P., Aglietta, M., Albury, J. M., et al. 2022, ApJ, 935, 170
Alves Batista, R., Biteau, J., Bustamante, M., et al. 2019, FrASS, 6, 23
Andringa, S., Conceicao, R., & Pimenta, M. 2011, APh, 34, 360
Ave, M., Hinton, J. A., Vazquez, R. A., Watson, A. A., & Zas, E. 2000, PhRvL, 85, 2244
Ave, M., Bohacova, M., Curry, E., et al. 2013, APh, 42, 90
Bonifazi, C. 2009, NuPhS, 190, 20
Coleman, A., Eser, J., Mayotte, E., et al. 2023, APh, 147, 102794
Dawson, B. 2020, ICRC (Madison), 36, 231
Dembinski, H., Billoir, P., Deligny, O., & Hebbeker, T. 2010, APh, 34, 128
Gaisser, T. K., & Hillas, A. M. 1977, ICRC (Plovdiv), 8, 353
Galbraith, W. 1958, Extensive Air Showers (Oxford: Butterworths), 185
Greisen, K. 1956, Progress in Cosmic Ray Physics, Vol. 3 (Amsterdam: North-Holland Publishing), 1
Greisen, K. 1960, ARNPS, 10, 63
Hillas, A. M. 1977, Acta Phys. Acad. Sci. Hung. Suppl, 29, 355
Hillas, A. M., Hollows, J., & Hunter, H. 1971, ICRC (Hobart), 3, 1001
Kamata, K., & Nishimura, J. 1958, PThPS, 6, 93
Linsley, J., & Scarsi, L. 1962, PhRv, 128, 2384
Luce, Q., Roth, M., Schmidt, D., & Veberic, D. 2022, ICRC (Berlin), 37, 435
Mollerach, S., & Roulet, E. 2018, PrPNP, 98, 85
Mostafá, M. A. 2005, ICRC (Pune), 29, 369
Newton, D., Knapp, J., & Watson, A. 2007, APh, 26, 414
Schmidt, T. 2010, PhD thesis, Karlsruhe Institute of Technology
Unger, M., Dawson, B. R., Engel, R., Schussler, F., & Ulrich, R. 2008, NIMPA, 588, 433
Valiño, I., Alvarez-Muñiz, J., Roth, M., Vazquez, R. A., & Zas, E. 2010, APh, 32, 304
Yushkov, A. 2019, ICRC (Madison), 36, 482